INSTITUTE OF PHYSICS PUBLISHING JOURNAL OF PHYSICS D: APPLIED PHYSICS

J. Phys. D: Appl. Phys. **38** (2005) R357–R379 doi:10.1088/0022-3727/38/22/R01

TOPICAL REVIEW

The behaviour of nanostructured magnetic materials produced by depositing gas-phase nanoparticles

C Binns[1], K N Trohidou[2], J Bansmann[3], S H Baker[1], J A Blackman[4], J-P Bucher[5], D Kechrakos[2], A Kleibert[3], S Louch[1], K-H Meiwes-Broer[3], G M Pastor[6], A Perez[7] and Y Xie[4]

[1] Department of Physics and Astronomy, University of Leicester, Leicester LE1 7RH, UK
[2] Institute of Materials Science, NCSR 'Demokritos', 153-10 Aghia Paraskevi, Attiki, Greece
[3] Institut für Physik, Universität Rostock, Universitätplatz 3, 18051 Rostock, Germany
[4] Department of Physics, University of Reading, Whiteknights, Reading RG6 6AF, UK
[5] IPCMS, 23 rue du Loess BP43, 67034 Strasbourg Cedex 2, France
[6] IRSAMC, Université Paul Sabatier, 118 rte de Narbonne, 31062 Toulouse Cedex 4, France
[7] LPMCN, Université Claude-Bernard Lyon 1, Bâtiment 203 La Doua 43, bd du 11 novembre 1918, 69622 Villeurbanne Cedex, France

Received 4 October 2004, in final form 31 August 2005
Published 7 November 2005
Online at stacks.iop.org/JPhysD/38/R357

Abstract

Depositing pre-formed gas-phase nanoparticles, whose properties can be widely varied, onto surfaces enables the production of films with designed properties. The films can be nanoporous or, if co-deposited with an atomic vapour, granular, allowing independent control over the size and volume fraction of the grains. This high degree of control over the nanostructure of the film enables the production of thin films with a wide variety of behaviour, and the technique is destined to make a significant contribution to the production of high-performance magnetic materials. Here we review the behaviour of magnetic nanoparticle assemblies on surfaces and in non-magnetic and magnetic matrices deposited from the gas phase at densities from the dilute limit to pure nanoparticle films with no matrix. At sufficiently low volume fractions ($\sim$1%), and temperatures well above their blocking temperature, nanoparticle assemblies in non-magnetic matrices show ideal superparamagnetism. At temperatures below the blocking temperature, the magnetization behaviour of both Fe and Co particles is consistent with a uniaxial intra-particle magnetic anisotropy and an anisotropy constant several times higher than the bulk magnetocrystalline value. At relatively low volume fractions ($\geqslant$5%) the effect of inter-particle interactions becomes evident, and the magnetization behaviour becomes characteristic of agglomerates of nanoparticles exchange coupled to form magnetic grains larger than a single particle that interact with each other via dipolar forces. The evolution of the magnetic behaviour with volume fraction is predicted by a Monte-Carlo model that includes exchange and dipolar couplings. Above the percolation threshold the films become magnetically softer, and films of pure clusters have a magnetic ground state that obeys the predicted magnetization behaviour of a correlated super-spin glass characteristic of random anisotropy materials. Magnetic nanoparticles in non-magnetic matrices show giant magnetoresistance behaviour, and the magnetotransport in deposited nanoparticle films is reviewed. Assembling Fe nanoparticles in Co matrices and vice versa is a promising technique for producing magnetic materials with a saturation magnetization that exceeds the Slater–Pauling limit. Structural studies reveal that the particles' atomic

structure is dependent on the matrix material, and it is possible to prepare Fe nanoparticles with an fcc structure and, unusually, Co particles with a bcc structure. We also look to the future and discuss applications for materials made from more complex bi-metallic and core–shell nanoparticles.

(Some figures in this article are in colour only in the electronic version)

1. Introduction

The fascination with gas-phase nanoparticles or 'clusters', containing a few to a few thousand atoms and diameters in the range 1–5 nm, dates back 30 years. Using clusters it has been possible to watch how fundamental properties of matter develop as a substance is built atom by atom from the monomer. The highlights include the discovery of the magic numbers of atoms for especially stable cluster configurations, originally in Xe clusters [1] and later in Na clusters [2]. A triumph was the discovery that in the case of Na magic numbers were related to the completion of electronic rather than atomic shells within a liquid drop model. This shed light on unresolved questions in nuclear physics such as the existence of the predicted 'supershells' [3, 4]. The importance of gas-phase clusters in producing novel materials arises from their size-dependent properties that are distinct from both the atomic and bulk states.

In the last decade there has been an increasing emphasis on exploiting the size-dependent behaviour of gas-phase clusters to produce nanostructured materials with 'designed' properties by depositing the clusters on surfaces. These can be co-deposited in conjunction with an atomic vapour of a matrix material [5] to produce granular films in which the grain size and volume fraction can be independently varied. A simplistic view of the process is shown in figure 1. The flexibility of control increases if the clusters are further functionalized in the gas phase by making them out of more than one material or producing core–shell clusters, for example, by a controlled oxidation [6, 7]. Still further versatility is shown by post-processing (heating, oxidation [8]) or depositing onto patterned substrates allowing the formation of arrays of quantum dots with tailored properties [9].

This ability to control the nanostructure is especially important in magnetic films, for example, optimizing the giant magnetoresistance (GMR) of nanogranular films by embedding size-selected magnetic nanoparticles in non-magnetic matrices [10, 11]. The co-deposition technique shown in figure 1 is also able to produce granular mixtures of miscible materials, for example, granular Fe–Co by co-depositing Fe nanoparticles in Co matrices or vice versa. Nanogranular Fe–Co is predicted to have a higher magnetization than homogeneous Fe–Co alloys and thus exceed the Slater–Pauling (SP) limit [12]. Recently ultra-high density magnetic recording tape media have been produced by depositing CoPt nanoparticles, whose properties were optimized in the gas phase, onto polymer substrates [13].

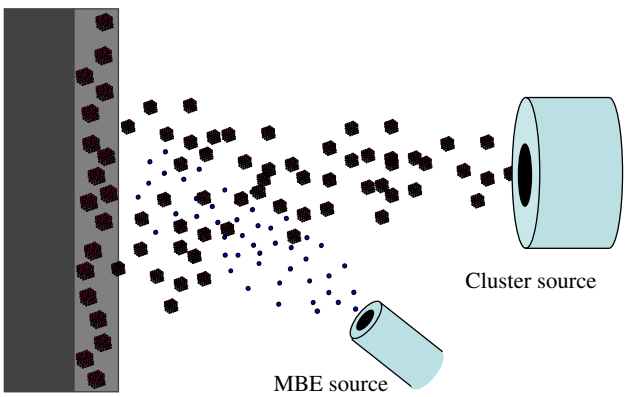

Figure 1. Formation of a cluster-assembled film by co-deposition of gas-phase nanoclusters and an atomic vapour from a conventional deposition source.

Although the metallurgy of cluster-deposited films would appear trivial, this is superficial as the reality is a rich complexity of structure and magnetic behaviour. For example, the atomic structure remains largely an open question even for the particles in the gas phase. When they are embedded in matrices the structure and morphology are modified and become dependent on the matrix material. At very low volume fractions, nanoparticle assemblies are superparamagnetic, but as the volume fraction is increased contact between the nanoparticles produces a strong exchange interaction and the effective particle size increases. Although the nature of the interfaces, for example, the degree of intermixing, is another open question the effective increase in particle size is clearly seen in the magnetic behaviour. These agglomerates interact via dipolar forces and the assembly no longer follows a simple superparamagnetic magnetization. When the volume fraction is increased beyond the percolation threshold the frustration between the nanoscale random anisotropy and the exchange interaction produces spin glass like behaviour and a significant magnetic softening. Pure cluster films, even though they are composed of a single element, have a different magnetic behaviour to conventional thin films produced by depositing atoms. For example, they do not form domains but minimize the magnetostatic term by having a magnetization that smoothly changes orientation with position [14].

Here we review the magnetic behaviour of cluster-assembled films starting with the simplest case of isolated particles in a matrix and following the evolution of the magnetic behaviour with particle volume fraction all the way through to pure cluster films. Section 2 presents what is known about the structure and morphology of gas-phase nanoparticles deposited on surfaces and embedded in matrices. Section 3 reports the measured magnetic behaviour of isolated nanoparticles at low volume fractions. The evolution of the magnetic behaviour with nanoparticle volume fraction is presented in section 4. For densities below the percolation threshold the results are interpreted with the aid of a Monte-Carlo (MC) model, while the behaviour of pure Fe and Co cluster films is discussed with reference to a random anisotropy model. Section 5 presents magnetotransport results from

cluster-assembled films and their analysis using the MC model. Section 6 discusses the prospects for producing high-moment soft films by cluster assembly. Finally, section 7 reports recent results on bi-metallic and core–shell gas-phase nanoparticles and their magnetic properties. The discussion throughout is restricted to clusters whose impact energy on the substrate corresponds to the 'soft-landing' regime of $\ll$1 eV/atom so that the impact with the substrate does not disrupt the atomic structure of the cluster structure but may induce a degree of flattening. Altering the cluster kinetic energy outside this regime can be considered as an additional parameter to modify the films' properties [15]. The majority of the work presented here is from the research conducted during the Framework 5 European Research and Technological Development project 'AMMARE' (Advanced Materials for Magnetic Recording).

2. Structure and morphology of deposited nanoparticle assemblies

2.1. Morphology of films produced by depositing clusters

The morphology of cluster-deposited films depends on both the cluster and substrate materials and, within the soft landing regime, varies from a random paving by individual clusters, when diffusion is limited, to large ramified islands composed of clusters when the cluster diffusion is significant. In the case of some simple metals, for clusters below a certain size, complete liquid-drop-like coalescence occurs to produce large particles. Case studies of all these different growth modes have been reported by several groups [16–20] and the data have been analysed using the deposition–diffusion–aggregation (DDA) model [20]. Changes in growth mode have been demonstrated as a function of cluster deposition energy [21] and of the density of substrate defects [19].

In the case of transition metal clusters like Fe or Co, only the random paving type of growth appears to occur. An example is shown in figure 2(*a*), which displays an *in situ* scanning tunnelling microscope (STM) image of Fe clusters deposited onto Si(111) in ultra-high vacuum (UHV). Figure 2(*b*) shows a transmission electron microscope (TEM) image of Fe clusters deposited onto amorphous carbon, and both images reveal a random paving morphology despite the different substrates. Although not every type of substrate has been studied by direct imaging techniques, the magnetic data to be presented in the next section shows that at low cluster densities the behaviour is consistent with a collection of isolated particles with the same size as those deposited. This is true for a wide range of substrates including highly-oriented pyrolitic graphite (HOPG), organic materials and various metals, so it is reasonable to assume that films produced by depositing magnetic transition metal clusters always grow as a random paving by the nanoparticles. The magnetic data also indicate that the anisotropy axes are randomly oriented, so it appears that films grow by clusters landing with a random orientation of their crystallographic axes at random positions on the substrate, where they stick.

In thick cluster films in which there are many layers of the deposited clusters, the effective particle size, as indicated by the magnetic data, is much larger than a single deposited nanoparticle. Large area AFM images, such as the one shown in figure 3(*a*) obtained from a 40 nm thick film of deposited Fe clusters on Si, also appear to indicate large feature sizes. Recent high-resolution images obtained in non-contact mode, however, (figure 3(*b*)) indicate that the individual deposited clusters can still be made out within the larger scale morphology. Thus the deposited particles, when they are in contact, are exchange coupled and behave magnetically as larger particles, but the crystalline orientation still changes randomly on the length scale of a single deposited cluster (∼2–3 nm).

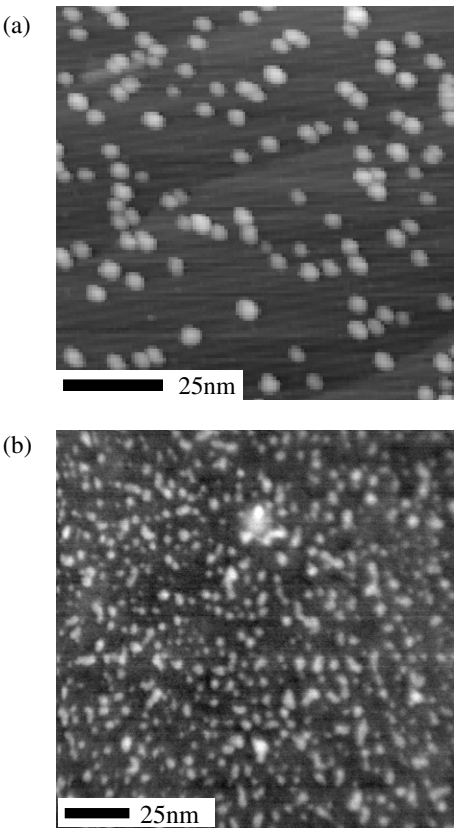

Figure 2. (*a*) *In situ* STM image of Fe clusters deposited on Si(111). (*b*) *Ex situ* TEM image of Fe clusters deposited on amorphous carbon and capped with amorphous carbon.

2.2. Atomic structure of supported clusters

High-resolution TEM images of isolated Co and Fe-clusters embedded in amorphous carbon (a-C) from the gas phase are shown in figure 4. The Fe particle (figure 4(*a*)) has a dodecahedral shape and an atomic bcc structure, while the Co particle (figure 4(*b*)) is a truncated octahedron and has an fcc atomic structure. The shapes of both particles are consistent with the minimum energy morphologies predicted by Wulff's construction [22].

Amorphous carbon matrices, which are highly transparent to energetic electrons, are useful for obtaining TEM images but are not very interesting for technological applications where generally the nanoparticles are embedded, by co-deposition, within a metal film. For nanoparticles in a metal matrix, extended x-ray absorption fine structure

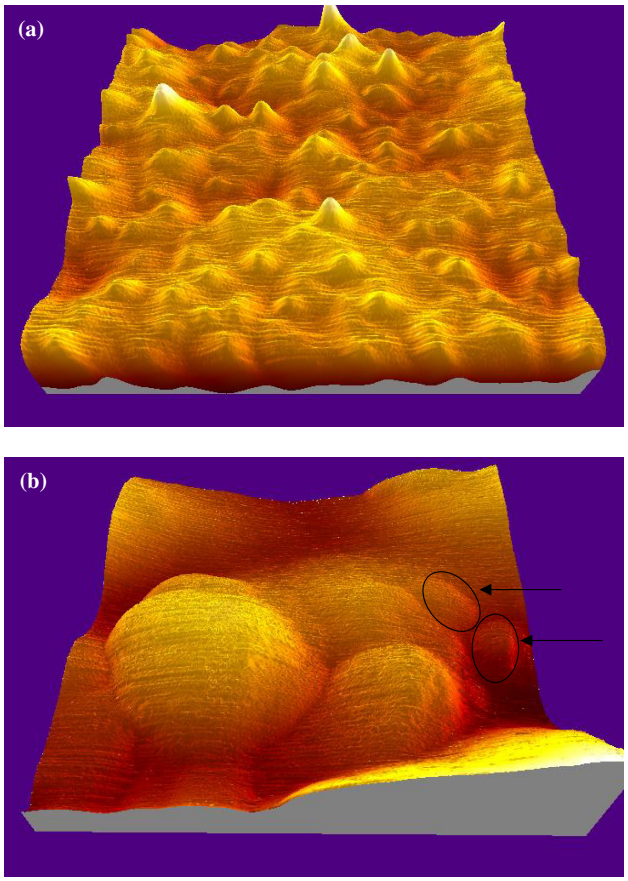

Figure 3. (*a*) Non-contact AFM image (900 nm × 900 nm) of 40 nm thick film of Fe clusters with a mean diameter of 2 nm deposited on Si and capped with a 3 nm thick film of amorphous carbon. (*b*) High-resolution (50 nm × 50 nm) image of the sample in (*a*) showing features with the size of the individual deposited particles (after accounting for tip convolution).

(EXAFS) measurements are a powerful method of obtaining atomic structures. They yield inter-atomic distances out to fourth nearest neighbours (NN) between different chemical combinations of atoms. Table 1 shows the results of an EXAFS study, using the SRS at Daresbury Laboratory [23], of samples of Fe nanoparticles embedded in various matrices with a range of volume fractions using the co-deposition technique (figure 1). The particle size distribution was log–normal with a median diameter of 1.85 nm (280) atoms. An interesting picture emerges, that is, the atomic structure of the Fe nanoparticles is bcc (Ag and Co matrices), fcc (Cu matrix) or a mixture of both (a-C matrix). The structure of the isolated clusters does not change if the volume fraction is increased to beyond the percolation threshold. It is clear that epitaxy with the metal matrices imposes a structure on the clusters. Thus the excellent lattice match between bcc Fe and fcc Ag produces a bcc structure for the Fe clusters, while the good lattice match between fcc Cu and fcc Fe yields fcc clusters. In a-C matrices where the clusters have no epitaxial relationship with the matrix the Fe particles are found in both fcc and bcc phases. It is tempting to associate the smallest clusters in the size distribution with the more closely packed fcc phase and the larger clusters with the bcc phase. It is likely that the atomic

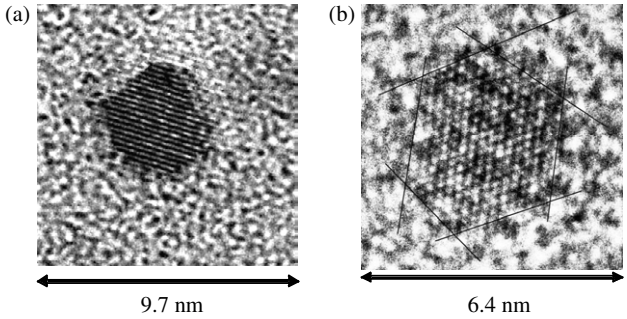

Figure 4. High resolution TEM images of (*a*) an isolated bcc Fe cluster and (*b*) an isolated fcc Co cluster embedded in amorphous carbon. The dodecahedral and truncated octahedral shapes, respectively, are consistent with the minimum energy morphologies predicted by Wulff's constructions [21].

structure of the Fe clusters in the a-C matrix is the same as when they are in the gas-phase. Films of Fe clusters embedded in Co are an important material for the production of high-moment films as reported in section 6.

The measurements were also carried out for Co clusters with a similar size distribution embedded in Ag and Fe matrices [24], and the results of the analysis are shown in table 2. The Co clusters in Ag show a close-packed structure, but the measurements were unable to distinguish between the fcc and hcp phases. A surprising result, however, is that the Co clusters embedded in Fe have the bcc structure. It is highly unusual to find bcc Co and this has significant implications for its magnetic behaviour. In general, the interface of clusters embedded in the noble metals was sharp with some evidence of intermixing in the case of transition metal matrices. Even for these small clusters in a miscible transition metal matrix, however, there always remains a pure elemental cluster core. This justifies the assertion in section 1 that the cluster/atom co-deposition technique is able to produce nanogranular mixtures of miscible metals.

An EXAFS study carried out at the LURE synchrotron on isolated Co clusters embedded in metal matrices including Ag, Pt and Nb focused on the degree of intermixing at the cluster/matrix boundary [25, 26]. This is revealed by comparing the number of chemically distinct NNs with a model for a given cluster size. The mean size of the Co clusters was the same as that used for the high resolution TEM image shown in figure 4(*b*), that is, a diameter of 3.4 nm (1289 atoms). For all the matrices, the Co atomic structure was found to be close-packed but fcc rather than the bulk hcp structure. Assuming the Co morphology and cluster size shown in figure 4(*a*) the co-ordination numbers $N_{Co–Co}$ and $N_{Co–M}$ (where M stands for 'matrix', i.e. Ag, Pt or Nb) can be modelled and is shown in table 3. The Co–Co co-ordination includes the core (dense Co) part and the 'disturbed', i.e. more diffuse Co with a larger separation in the case where interfacial mixing occurs. The measured data is shown in table 4, and comparison with table 3 reveals that the interface is sharp with no intermixing in the case of Co clusters embedded in Ag matrices but that there are one and two mixed atomic layers in Pt and Nb matrices, respectively.

Table 1. Structural parameters of Fe clusters embedded in various matrices.

Matrix material containing Fe clusters	Volume fraction (%)	r_1 (Å)	r_2 (Å)	r_3 (Å)	r_4 (Å)	Structure of Fe clusters
Silver	5	2.49 ± 0.01	2.85 ± 0.01	4.10 ± 0.01	4.79 ± 0.01	Bulk bcc structure
	40	2.49 ± 0.01	2.85 ± 0.01	4.08 ± 0.02	4.77 ± 0.01	
Bulk bcc Fe		2.49	2.87	4.06	4.76	
Copper	6	2.53 ± 0.02	3.57 ± 0.02	4.43 ± 0.02	5.28 ± 0.02	γ-Fe fcc structure with slightly reduced lattice parameter
Amorphous carbon	4	2.49 ± 0.01	2.56 ± 0.02			Mixture of bcc and fcc phases
	40	2.46 ± 0.01	2.57 ± 0.01			
Cobalt	9	2.49 ± 0.02	2.84 ± 0.02	4.06 ± 0.02	4.78 ± 0.02	Bulk bcc structure

Table 2. Structural parameters of Co clusters embedded in Ag and Fe matrices.

Matrix material containing Co clusters	Volume fraction (%)	r_1 (Å)	r_2 (Å)	r_3 (Å)	r_4 (Å)	Structure of Co clusters
Silver	5	2.49 ± 0.02	3.49 ± 0.02	4.04 ± 0.02	4.36 ± 0.02	Close packed hcp or fcc
Iron	7	2.45 ± 0.02	2.86 ± 0.02	4.06 ± 0.02	4.73 ± 0.02	bcc Fe structure

Table 3. Coordination numbers of Co-atoms in a cluster consisting of a fcc-truncated octahedron embedded in a matrix M. The size of the cluster considered in this case is 3.4 nm (1289 atoms, $m = 5$ layers). For clusters of this size the co-ordination numbers predicted for the formation of 0, 1, 2 or 3 intermixed CoM-layers are shown.

Type of the Co–M interface for a Co-cluster model embedded in a matrix M	$N_{Co–Co}$ Total = core + disturbed	$N_{Co–M}$ Total
Epitaxy Co/M with an abrupt interface	10.6 = 10.6 + 0	1.4
One diffuse layer at the Co–M interface	8.8 = 6.5 + 2.3	3.2
Two diffuse layers at the Co–M interface	6.5 = 2.9 + 3.6	5.5
Three diffuse layers at the Co–M interface	4.6 = 1.6 + 3	7.4

Table 4. Coordination numbers of Co atoms in different matrices, $N_{Co–M}$ (M = Ag, Pt or Nb), as deduced from the fits of the EXAFS spectra.

Sample	$N_{Co–Co}$ Total = core + disturbed	$N_{Co–M}$ Total	Degree of intermixing at interface
Co-clusters/ Ag-matrix	11	1	Sharp interface
Co-clusters/ Pt-matrix	9.6	2.4	1 atomic layer mixed
Co-clusters/ Nb-matrix	7	5	2 atomic layers mixed

3. Magnetic behaviour of isolated Fe and Co nanoparticles

3.1. Magnetometry of isolated nanoparticle impurities in Ag matrices

To understand the magnetic properties of dense interacting assemblies of nanoparticles we need to determine the behaviour of the individual particles. This can be probed by magnetometry measurements in dilute (1–2% volume fraction) assemblies of magnetic clusters embedded in non-magnetic matrices prepared by co-depositing the clusters and the matrix as in figure 1.

Figure 5(*a*) shows in-plane magnetic isotherms in the temperature range 50–300 K (symbols) from an assembly of un-filtered Fe clusters embedded in Ag with a volume fraction of 1% (Fe_1Ag_{99}) by the co-deposition technique (figure 1) [27, 28]. The upper left inset shows the same data plotted versus H/T, and it is evident that the magnetization isotherms scaled thus follow a universal curve. This feature, the lack of hysteresis and the observation that the fitted particle size, assuming the curves are Langevin functions, is independent of temperature are the three criteria to be satisfied for confidence that the samples are superparamagnetic [27].

Since the assembly displays ideal superparamagnetism in the range 50–300 K, the size distribution of the clusters can be obtained by fitting a set of Langevin functions to every isotherm. Each fitted Langevin function has a different argument (particle size) and the set of fitting variables are the amplitudes of the functions. Ten size bins were used in the range 0.5–8 nm, and the average amplitude as a function of particle size, obtained by fitting the data at all temperatures, is shown in the bottom inset in figure 5(*a*). The calculated magnetization curves are displayed as lines, and the fit is excellent in every case. The size distribution is the usual asymmetric shape and has been fitted to a log–normal distribution of particle diameters, d:

$$f(d) \propto \exp\left(-\frac{((\ln d) - \mu)^2}{2\sigma^2}\right), \qquad (1)$$

where μ and σ in equation (1) are, respectively, the mean and standard deviation of $\ln d$ and are treated as fitting variables. The most probable diameter is thus $\exp(\mu)$ and, as pointed out by O' Grady and Bradbury [29], the standard deviation of particle diameters, σ_d, is given from the fitted values of μ

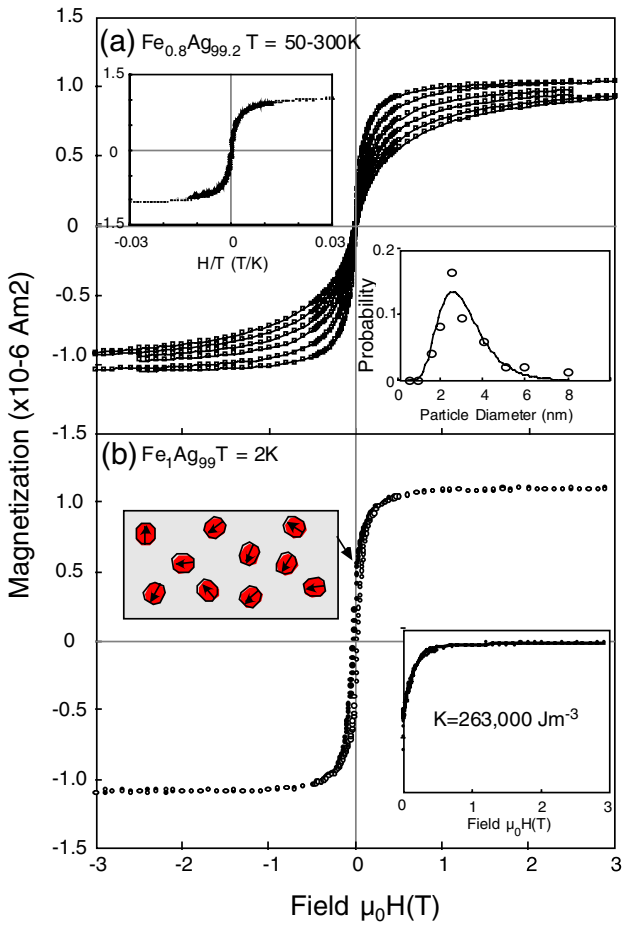

Figure 5. Magnetization isotherms in the range 50–300 K of an Fe_1Ag_{99} cluster-assembled film (□) compared with fits by Langevin functions (——) with a size distribution represented by 10 size bins in the range 0.5–8 nm. The lower inset shows the average probability of each bin for the optimum fit to curves at temperatures >50 K (○) and the corresponding log–normal distribution (——) fitted by equation (1). The fit gives a most probable diameter of 2.57 nm and a standard deviation of particle diameters, from equation (2), of 1.03. The upper left inset shows the magnetization data plotted versus H/T demonstrating the universal scaling expected for a superparamagnetic assembly. (*b*) In plane magnetization isotherms at 2 K of Fe_1Ag_{99} sample: (●) field sweeping down, (○) field sweeping up. The lower right inset shows the decay from saturation (●) compared with a calculation (——) assuming a random distribution of uniaxial anisotropy axes (equation (3)). The best fit anisotropy constant is displayed in the inset. The upper left inset shows schematically the random orientation direction averaged over a hemisphere giving 50% remanence.

and σ by

$$\sigma_d = \exp\left(\mu + \frac{\sigma^2}{2}\right)(\exp(\sigma^2) - 1)^{1/2}. \qquad (2)$$

Fitting equation (1) to the measured size distribution (bottom inset in figure 5(*a*)) yields a most probable diameter of 2.57 nm with a standard deviation of particle diameters, from equation (2), of $\sigma_d = 1.03$. The median diameter, d_m, obtained by finding the value of d at which the integral of the distribution given by equation (1) is equal on either side of d_m, is 3.0 nm. This is taken as the representative size for further analysis. The size distribution thus obtained by magnetometry is similar to that obtained by direct STM imaging of deposited cluster films produced by the same cluster source [27] confirming that the clusters are isolated in the film.

As shown in figure 5(*b*), at 2 K the magnetic isotherm of the Fe_1Ag_{99} sample develops hysteresis showing that some of the clusters within the size distribution are magnetically blocked with the proportion depending on the symmetry of the anisotropy. As demonstrated by Jamet *et al* [30], for embedded Fe nanoparticles of about the same size, because of the high surface to volume ratio (~40% of the atoms are on the surface layer), these small particles are dominated by surface anisotropy. Cubic anisotropy or any symmetry higher than uniaxial would only occur in clusters containing magic numbers of atoms. According to Xie and Blackman [31] adding a few atoms to one of the facets induces uniaxial anisotropy. There are only a few magic numbers in the entire size distribution, and so the vast majority of the clusters are expected to show uniaxial anisotropy. Even in the case of magic numbers, the process of depositing and embedding the clusters may induce stresses that lower the symmetry of the anisotropy. The remanence, M_r, of an assembly of blocked particles with uniaxial anisotropy is $M_r/M_s = 0.5$, if the directions of the anisotropy axes are randomly distributed over three dimensions, and $M_r/M_s = 0.71$, if they are distributed over two dimensions in the plane of the applied field. The measured remanence is just below 0.5 and thus closest to the case for uniaxial anisotropy axes randomly distributed over 3D. The slight discrepancy is probably due to the smallest clusters in the distribution remaining unblocked at 2 K. For particles with a uniaxial anisotropy randomly oriented in 3D the magnetization between saturation and remanence is obtained at each field by minimizing over all alignments of the anisotropy axes, the intra-particle energies:

$$E_\phi = KV\sin^2(\theta - \phi) - \mu B\cos\phi, \qquad (3)$$

where K is the anisotropy constant, V is the particle volume and θ and ϕ are the angles between the applied field and the anisotropy axis and particle magnetization, respectively. The inset in figure 5(*b*) compares the curve, calculated thus, with the data, and it is evident that this simple model reproduces the data accurately. So in zero field the system is a collection of static, randomly aligned cluster giant moments, each pointing along the local anisotropy axis. The anisotropy constant is a parameter of the fit and optimizes at $K = 2.63 \times 10^5\,\mathrm{J\,m^{-3}}$ (~3 meV/atom). Note that this includes all anisotropy terms including the surface, magnetocrystalline, shape and stress contributions. A previous measurement with the applied field perpendicular to the film plane revealed similar behaviour with a slightly higher anisotropy constant [28], which was attributed to a degree of 'flattening' of the clusters on landing.

Magnetic isotherms from a Co_2Ag_{98} cluster assembled film in the temperature range 50–300 K are shown in figure 6(*a*) (symbols) along with the Langevin fits using the procedure described above (lines) [28]. In this case, as seen in the upper left inset, a departure from the H/T scaling and thus ideal superparamagnetism is observed below 150 K, which is attributed to a higher anisotropy of the Co clusters (see below). Thus the basic assumption of superparamagnetism, that is, a nearly isotropic magnetic moment, will require a higher temperature to be realized. The size distribution can be

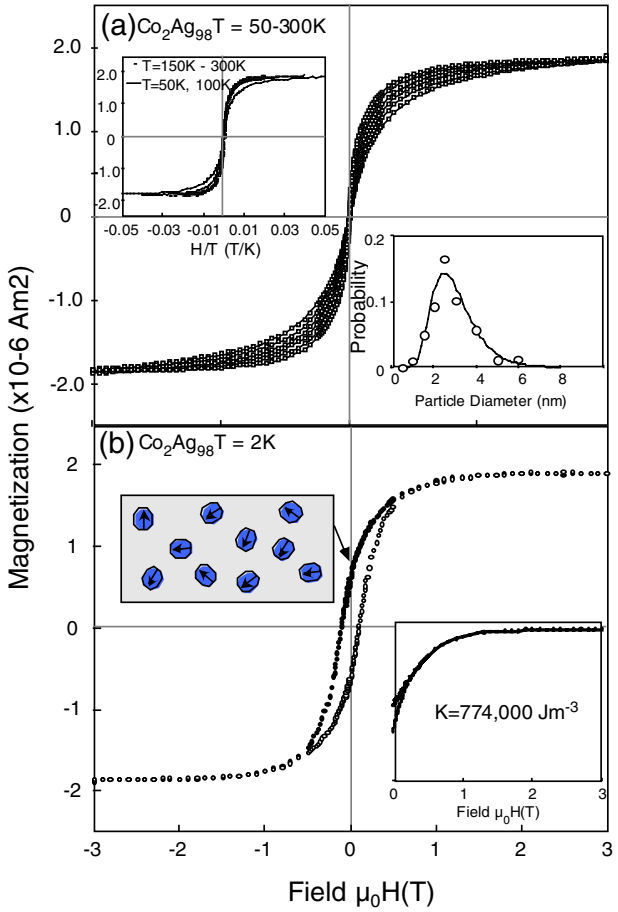

Figure 6. Magnetization isotherms in the range 50–300 K of an Co_2Ag_{98} cluster-assembled film (□) compared with fits by Langevin functions (——) with a size distribution represented by 10 size bins in the range 0.5–8 nm. The lower inset shows the average probability of each bin for the optimum fit to curves at temperatures >150 K (○) and the corresponding log–normal distribution (——) fitted by equation (1). The fit gives a most probable diameter of 2.51 nm and a standard deviation of particle diameters, from equation (2), of 0.90. The upper left inset shows the magnetization data plotted versus H/T. In this case, unlike Fe, the 50 and 100 K isotherms do not follow the universal H/T scaling indicating a departure from ideal superparamagnetism below 150 K. (*b*) In plane magnetization isotherms at 2 K of Co_2Ag_{98} sample: (●) field sweeping down, (○) field sweeping up. The lower right inset shows the decay from saturation (●) compared to a calculation (——) assuming a random distribution of uniaxial anisotropy axes (equation (3)). The best-fit anisotropy constant is displayed in the inset. The upper left inset shows schematically the random orientation direction averaged over a hemisphere giving 50% remanence.

obtained by Langevin fits as described above but restricted to the data obtained at $T \geqslant 150$ K. The result along with the fitted log–normal distribution (equation (1)) is shown in the lower inset in figure 6(*a*). Applying the same analysis as for the Fe clusters gives a most probable Co particle diameter of 2.51 nm and a standard deviation of diameters (equation (2)) of 0.90. In this case the median diameter is 2.8 nm.

The low temperature isotherms from the isolated Co clusters in Ag are shown in figure 6(*b*) and again a remanence of slightly less than 50% is found. As discussed earlier for Fe clusters, Co nanoparticles are also expected to show a uniaxial anisotropy, and the remanence indicates that the clusters are randomly oriented over 3D. The approach to saturation can thus be modelled using equation (3) and this is compared to the data in the inset in figure 6(*b*). The anisotropy constant that optimizes the fit is about 3 times larger than found in the Fe cluster assembly, which explains why higher temperatures are required to observe ideal superparamagnetism in Co cluster assemblies.

3.2. MC model of nanoparticle assemblies

A MC model developed to describe the behaviour of cluster-assembled films has been reported [27]. It considers N identical spherical magnetic particles with a diameter D and volume V_0 inside a cubic box of edge length L. For simplicity, the space inside the box is discretized by a simple cubic lattice with a lattice constant equal to the particle diameter. Particles are placed at random on the nodes of the lattice, thus overlap is avoided [32]. As dictated by the experimental results, the single-domain particles are assumed to have a randomly-oriented uniaxial anisotropy. The particles interact via long-range dipolar forces and short-range exchange forces, these only being included between neighbouring particles in contact. The total energy of the system is the sum of particle magnetic energies:

$$E_i = -\sum_i \varepsilon_i$$

in which the energy of the ith particle is

$$\varepsilon_i = h(\hat{\boldsymbol{S}}_i \cdot \hat{\boldsymbol{H}}) + k(\hat{\boldsymbol{S}}_i \cdot \hat{\boldsymbol{e}}_i)^2 + g\sum_j \frac{3(\hat{\boldsymbol{S}}_i \cdot \hat{\boldsymbol{R}}_{ij})(\hat{\boldsymbol{S}}_i \cdot \hat{\boldsymbol{R}}_{ij}) - (\hat{\boldsymbol{S}}_i \cdot \hat{\boldsymbol{S}}_j)}{R_{ij}^3} + J\sum_j (\hat{\boldsymbol{S}}_i \cdot \hat{\boldsymbol{S}}_j), \quad (4)$$

where $\hat{\boldsymbol{S}}_i$ and $\hat{\boldsymbol{e}}_i$ are unit vectors in the directions of the magnetic moment (spin) and anisotropy axis of the ith particle and $\hat{\boldsymbol{R}}_{ij} \cdot \boldsymbol{D}$ is the centre-to-centre distance between the particles. The energy parameters entering equation (4) are the Zeeman energy, μH, where $\mu = M_s V_0$, the dipolar energy, $g = \mu_0 \mu^2 / 4\pi D^3$, the anisotropy energy, $k = K V_0$, and the effective change energy, J. The anisotropy parameter can be obtained from the fits to the experimental magnetization curves as described in the previous section, and the exchange energy can be obtained by fitting the measured approach to saturation in dense interacting cluster assemblies as described in section 4. The equilibrium magnetic configuration of the system at a certain temperature and applied field is obtained by a MC simulation using the Metropolis algorithm [32]. The model predicts a percolation threshold at a volume fraction of 29% and that the dilute limit extends up to about 5%, where the probability of particles in contact is small. The intermediate volume fraction regime covers the range 5–25%. In all simulations it is assumed that the morphology of the Fe clusters does not change with volume fraction.

The simulation was tested for a dilute Fe_1Ag_{99} nanoparticle assembly similarly to the one shown in figure 5 using the corresponding fitted anisotropy (in this case 2.41×10^5 J m^{-3}). At such a low volume fraction the exchange parameter does not have a significant effect as the probability of finding two particles in contact is very low. The calculated full magnetization curve using the MC model is compared with

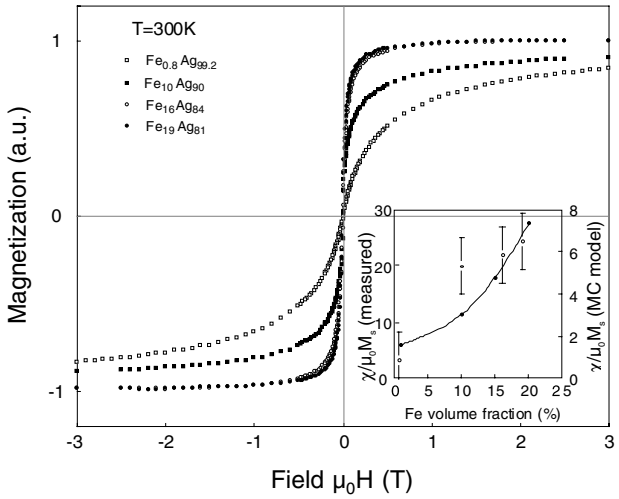

Figure 7. Magnetization isotherms at 300 K of films as a function of volume fraction in the intermediate range. The inset compares the measured initial susceptibility with that calculated by the MC simulation as a function of volume fraction (note the different scales).

the experimental data obtained at 2 K (i.e. below the blocking temperature) in figure 8 (top curve). It is observed that the model describes the data reasonably well and gives a good estimate of the coercive field (0.02 T). The main discrepancy is the loss of hysteresis at a lower field than observed in the data. This is attributed to the model describing each particle by a single average spin, whereas for isolated particles the surface spins need a higher field than the core to saturate because of the enhanced surface anisotropy. As shown in section 4 at higher concentrations where the inter-particle interactions are dominant the surface contribution is less important and the model gives even better agreement.

4. Evolution of magnetic behaviour with nanoparticle volume fraction

4.1. Volume fractions below the percolation threshold

The volume fraction in a cluster-assembled film for a given particle size can be adjusted simply by changing the relative deposition rates of the clusters and matrix material. The evolution of the magnetization curves at 300 K as a function of volume fraction for films containing 3 nm diameter Fe nanoparticles in Ag matrices is shown in figure 7 for volume fractions below the percolation threshold. The most noticeable feature is the increase of the low-field susceptibility as the cluster density increases. This is characteristic of larger particles and indeed it is possible to get good fits using Langevin functions with a higher supermoment than in the dilute film. It is, however, erroneous to treat these films as superparamagnetic with a volume fraction dependent cluster size. The magnetic isotherms do not scale with H/T, and Langevin fits to these curves give an optimum particle size that depends on the temperature of the fit. As pointed out by Allia *et al* [34], both these features violate the criteria for superparamagnetism.

The MC model can be applied to these samples, but for comparisons at room temperature it is important to point out some expected differences between the measured data and the simulation. In an MC simulation, due to the absence of true spin dynamics, the physical time does not enter directly, but 'time' is measured in Monte-Carlo steps (MCSs). The simulations applied in this case extend to 10^4 MCS per spin, which approximately corresponds to an observation time of 10^{-7} s [32]. Consequently, the MC simulation for the dilute sample (figure 6) predicts a much higher blocking temperature (∼32 K) than the experimental value of ∼5K. Comparing the measured and simulated data is thus similar to comparing measurements with widely different time scales, for example, dc magnetometry and Mössbauer spectroscopy. However, the MC simulation, because it mimics the role of thermal fluctuations, reproduces qualitatively the trend of the experimental data. The trend in the initial susceptibility as the volume fraction changes for the experimental data is plotted in the inset in figure 7 and compared with the prediction from the MC model. It is seen that there is qualitative agreement with the model. Theoretical modelling [35] and measurements [34] show that, without exchange, dipolar forces decrease the low field susceptibility emphasizing the importance of including exchange interactions to explain the behaviour of these samples.

The magnetic isotherms of the same samples as in figure 7 measured at 2 K are shown in figure 8. In each case the demagnetization from saturation is still well described using equation (3) (thick solid lines in figure 8), and the remanence is close to 50% indicating that at 2 K in the zero field the moments are frozen along randomly oriented axes averaged over 2π steradians in the direction of the most recent saturation. Here, however, the moments do not belong to individual deposited nanoparticles but to exchange-coupled aggregates of the nanoparticles. These are the relevant magnetic particles in samples with volume fractions between 5% and the percolation threshold. As before, a remanence of 50% indicates that the anisotropy of aggregates is uniaxial. The magnitude of the anisotropy of the aggregates, obtained by the fit to the data using equation (3), is lower in the $Fe_{10}Ag_{90}$ film than that found in the isolated clusters and decreases with increasing density of clusters. This is expected due to an averaging of the individual cluster anisotropies to produce a resultant value along the anisotropy axis of the whole aggregate. In addition a real decrease in the intracluster magnetocrystalline anisotropy may be expected as a result of a decreasing orbital moment with density as shown by previous XMCD measurements on exposed Fe clusters on graphite [36].

The complete magnetization curves obtained using the MC model as a function of volume fraction are indicated in figure 8 by the thin solid lines. The anisotropy value used was that of the isolated clusters (figure 5(*b*)) as is appropriate. If the model is working correctly it should predict the reduction of anisotropy of the aggregates due to the random orientation of the constituent nanoparticles. The good fit to the data indicates that this is the case. This also implies that the decreasing anisotropy constant in the films is mostly due to the averaging effect and not due to the measured reduction of the orbital moment. This is not surprising since the orbital moment will affect only the magnetocrystalline term and it is clear that this is a minor component. The relatively small contribution of the magnetocrystalline term to the

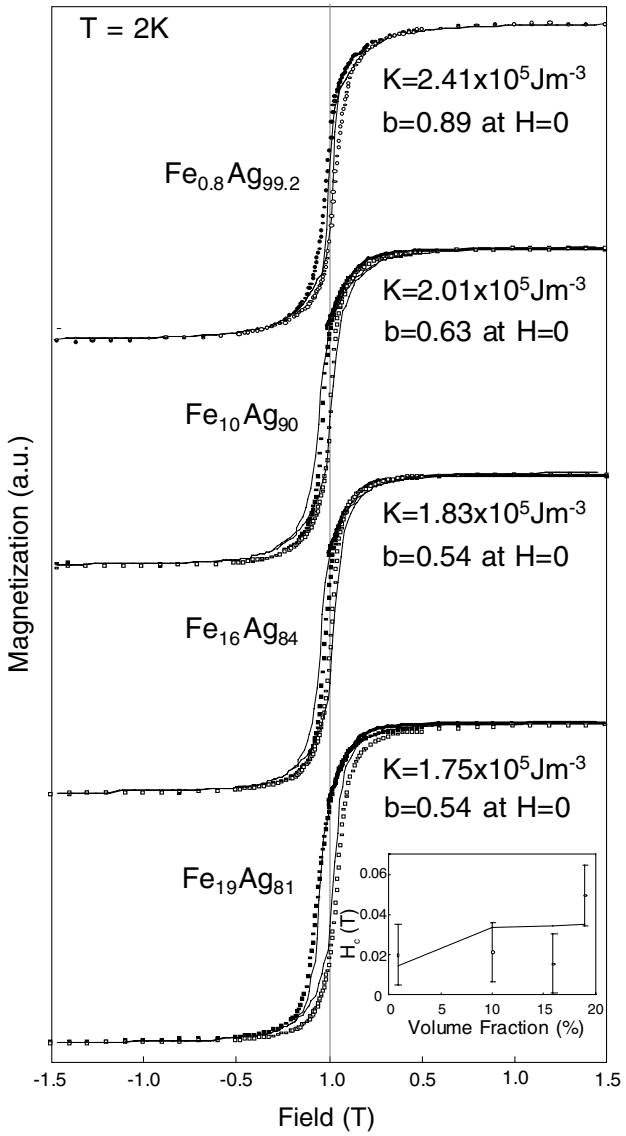

Figure 8. Isotherms at 2 K from samples with intermediate volume fractions below the percolation threshold. The symbols are the measured data and the thick lines are fits between saturation and remanence using equation (3) with the optimal value of the anisotropy constant shown. The thin solid lines are the MC simulations for the full isotherms with the predicted value of b at remanence shown. The inset compares the values of H_c obtained from the measurements and the MC simulation.

anisotropy of embedded clusters has been confirmed recently by direct micro-SQUID measurements of the switching field of individual nanoparticles [30]. The simulation also gives a good estimate of the coercive field and predicts the experimental observation of a slight increase with increasing Fe volume fraction. The large error bars for the experimentally determined values of H_c are due to uncertainties in the removal of the background slope from the raw data. The variation of H_c with volume fraction is due to the different character of the dipolar interactions in the system well below and close to the blocking temperature. For $T \ll T_b$, H_c is predicted to decrease with increasing volume fraction, while for $T \sim T_b$ it will increase. This is clearly the regime found in our samples. More fundamentally, it is evident that H_c is modified by interactions as it is observed to increase despite a decreasing anisotropy constant in the aggregates. This would be a contradiction in a non-interacting system.

The increased exchange coupling due to aggregation is indicated by the MC simulation via the global parameter:

$$b = \frac{1}{N}\sum_i \hat{\boldsymbol{S}}_i \cdot \hat{\boldsymbol{e}}_i, \tag{5}$$

that is, the fraction of projected moments along the local easy axes. A value of 1 indicates complete decoupling of clusters so that all moments are along local easy axes, and 0.5 will be found in the case where all neighbouring moments are aligned co-linearly by exchange. The values of b obtained from the MC simulations shown in figure 8 are indicated beside each magnetization curve. For the dilute cluster film (figure 6) it is found that $b = 0.89$ at $H = 0$ and $T = 2$ K but drops to 0.63 in the $Fe_{10}Ag_{90}$ sample and drops further towards the exchange coupled limit as the Fe cluster volume fraction increases. Note that this reduction in b indicates an increasing proportion of the deposited nanoparticles contained in exchange-coupled aggregates, whose total moments are randomly oriented in the zero field. This is consistent with the observation of an approximately 50% remanence in both the measured data and the MC simulations.

The exchange-coupled aggregates will interact with each other via dipolar forces, and some information on the size of the aggregates and their interaction can be extracted from the experimental data using a model proposed by Allia *et al* [34]. The dipolar interactions are characterized by a parameter, T^*, proportional to the rms dipolar energy, appearing in the denominator of a modified Langevin function analogous to the Curie–Weiss law; that is:

$$M = \mu N L\left(\frac{\mu H}{k(T+T^*)}\right), \tag{6}$$

where μ is the true particle (aggregate) moment. From this expression it can be shown that the true diameter d is related to the apparent (or wrong) diameter d_a, obtained by fitting simple (superparamagnetic) Langevin functions to the magnetization curves, by

$$d_a = \left(\frac{1}{1+T/T^*}\right)^{1/3} d. \tag{7}$$

As pointed out earlier, if one tries, erroneously, to fit Langevin functions to assemblies of nanoparticles in which there are interactions, it is usually possible to get a good fit but the size parameter that optimizes the fit becomes dependent on the temperature. This is a useful test to determine if the system really is superparamagnetic. Within the above model the size-dependence of the fitted (and wrong) size, however, can be used to extract the real size and the interaction parameter T^* using equations (6) and (7). The variation of d_a versus temperature is shown in figure 9 for the $Fe_{0.8}Ag_{99.2}$ and $Fe_{10}Ag_{90}$ samples already described. For the dilute cluster sample no significant variation with cluster size can be observed, and fits using equation (7) give T^* less than the single particle blocking temperature. For the 10% volume fraction sample the variation is well described by equation (7) and one obtains $T^* = 94$ K and a mean aggregate diameter of 5.7 nm. Thus, in the

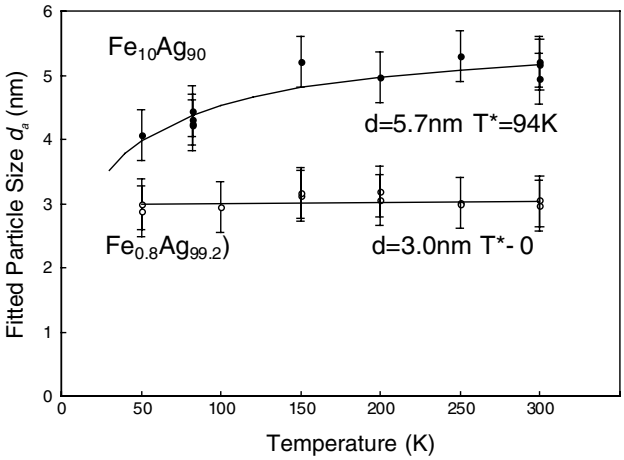

Figure 9. Median particle diameter d obtained by fitting unmodified Langevin functions to the magnetization curves taken at 50–300 K of the $Fe_{0.8}Ag_{99.2}$ (○) and $Fe_{10}Ag_{90}$ (●) samples. The variation of d_a versus T can be used to obtain the interaction parameter T^* and the true particle size, d, from equation (7).

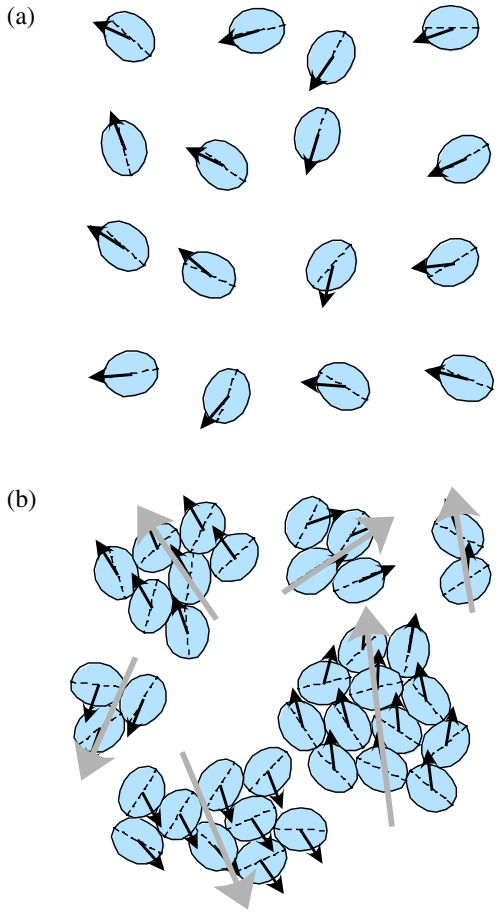

Figure 10. Schematic of Fe nanoparticle assemblies dispersed in Ag with a uniaxial anisotropy and a random orientation of the anisotropy axis at $T = 0$ and zero field. (*a*) 1% volume fraction: the MC model yields $b = 0.89$ (equation (5)), indicating that all the particle moments are oriented close to the local anisotropy axis. (*b*) 10% volume fraction: equations (7) indicates that the deposited nanoparticles from aggregates containing on average about 7 particles and the MC model gives $b = 0.63$, indicating that the aggregates are strongly exchange coupled to form single magnetic entities. The measured remanence of 50% shows that the aggregate moments are randomly oriented.

$Fe_{10}Ag_{90}$ sample, a typical aggregate consists of 6–7 of the deposited nanoclusters exchange coupled and behaving as individual larger particles. These interact via dipolar forces, the strength of which is characterized by T^*.

The development of the nanoparticle assembly and its magnetic ground state from a 1% volume fraction to a 10% volume fraction is shown schematically in figure 10. At a 1% volume fraction, each particle has its moment frozen close to the local (randomly oriented) anisotropy axis as indicated by a b parameter (equation (5)) of 0.89 given by the MC model. At 10% volume fraction, the model described by Allia *et al* [34] (equations (6) and (7)) shows that the nanoparticles form aggregates consisting on average of about 7 of the deposited clusters. The MC model indicates that these are strongly exchange coupled ($b = 0.63$) to form single magnetic entities, but the measured 50% remanence shows that the magnetic moments of the aggregates are randomly oriented.

Having thoroughly tested the MC model on manufactured nanoparticle assemblies it can be used to predict the behaviour of interacting assemblies with different dipolar, anisotropy and exchange parameters in equation (4) and reveal the role of the exchange and dipolar couplings. Figure 11(*a*) shows the behaviour of the remanence. At volume fractions above the dilute limit weak exchange forces enhance the remanence, as they favour ferromagnetic alignment of the moments. The effect of dipolar forces on the remanence depends on how the particles are distributed; for example, in a chain of particles the remanence is enhanced. With the arrangement of particles within the samples studied here, that is, a random 3D assembly, dipolar forces produce a suppression of the remanence with volume fraction and thus compete with the exchange forces. The value $g/k \sim 1$ defines the crossover from a dipolar- to an exchange-coupled assembly. Finally, in the dense limit ($x > 0.3$) exchange forces dominate producing bulk ferromagnetic behaviour.

As shown in figure 11(*b*) both types of interaction have a similar effect on the coercivity, namely a suppression of H_c with cluster density. The effects of the exchange and dipolar interactions are not always additive. This is clear in the case of coalesced clusters ($J/k \gg 1$). This behaviour is attributed to the strong random dipolar fields generated in the sample containing large, almost isotropic, coherent clusters. Due to these random fields an extra effective anisotropy is produced that enhances H_c.

4.2. Global anisotropy in nanoparticle films

Section 3.1 discussed the anisotropy of the isolated deposited particles, which was shown to be uniaxial. It has also been observed that the supported nanoparticles have a small in-plane coherent anisotropy [28] possibly due to a degree of flattening upon collision with the substrate. It is important, especially for applications, to know the orientation of the global magnetic anisotropy in strongly interacting films of clusters. Figure 12 shows how the remanence at 40 K of films of Fe nanoparticles with an average diameter of 2.2 nm (450 atoms) deposited on Cu and HOPG substrates varies with the cluster coverage [37]. The data were obtained using magnetic linear and circular

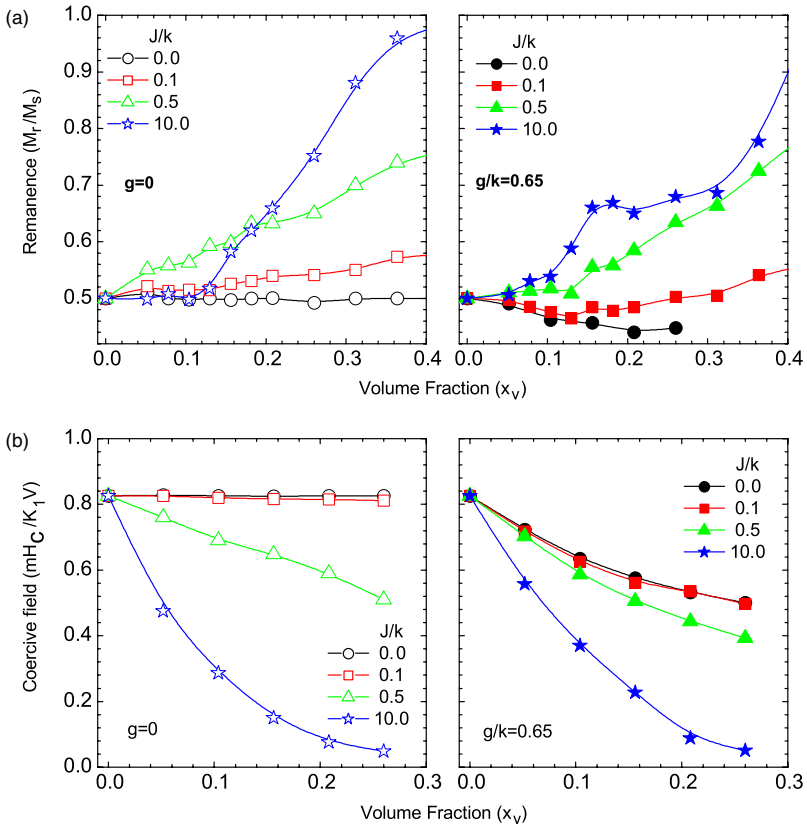

Figure 11. (*a*) Concentration dependence of remanence at low temperature ($k_BT/k = 0.01$). Left panel: exchange coupling only ($g = 0$). Right panel: exchange and dipolar coupling ($g/k = 0.65$). (*b*) Concentration dependence of coercivity at low temperature ($t/k = 0.01$). Left panel: exchange coupling only ($g = 0$). Right panel: exchange and dipolar coupling ($g/k = 0.65$).

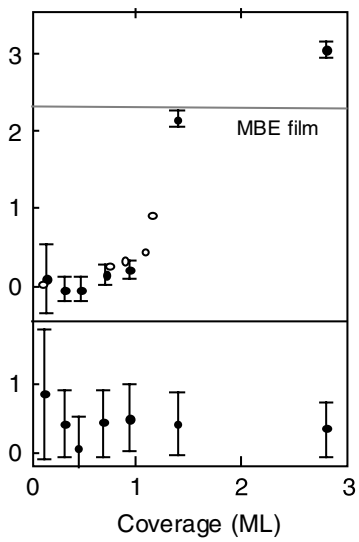

Figure 12. MCDAD (out-of-plane magnetization) and MLDAD (in-plane magnetization) signals versus coverage at 40 K for un-filtered Fe clusters with an average diameter of 2.2 nm (450 atoms) on HOPG (○) and Cu (●). The MLDAD signal for a 60 Å thick MBE-grown film deposited *in situ* onto HOPG is also shown.

dichroism in the angular distribution of Fe 3p photoelectrons (MLDAD and MCDAD) that measure, respectively, the in-plane and out of plane remanent magnetization. Prior to each measurement a field pulse with an amplitude of about 0.1 T was applied to the sample parallel or perpendicular to the surface. At low coverages, the samples are superparamagnetic at 40 K and thus have no magnetization without an applied field, but an in-plane remanence develops as the coverage increases and the clusters begin to interact. The films have no remanent component out of plane at any coverage showing that the global anisotropy of the film is always in-plane.

It is clear from a study of Co islands grown on Au(111) that the orientation of the film anisotropy is sensitive to the morphology of the film [38]. This work was on Co islands formed by Volmer–Weber growth rather than on deposited gas-phase nanoparticles but it revealed a switch from in-plane to out of plane anisotropy which was a result of a change in the Co island size. The Au(111) surface undergoes a well-characterized 'herringbone' reconstruction, the unit cell of which has dimensions 75 Å × 150 Å. Co atoms deposited on the reconstructed surface at 300 K have a diffusion length larger than the reconstruction unit cell and tend to form bilayer islands 7 nm across (∼1000 atoms) located at the corners of the unit cell (figure 13(*e*)). Growth at 30 K, on the other hand, at which the diffusion length is smaller than the reconstruction unit cell leads to a dense packing of very small islands each containing ∼10 atoms (figure 13(*f*)). Figures 13(*a*)–(*d*) show the longitudinal and polar Kerr rotations, for reflected polarized light, which are sensitive to, respectively, the in-plane and out of plane sample magnetization. It is evident that the dense array of large islands has an out of plane anisotropy while the film of smaller islands has its easy axis in-plane.

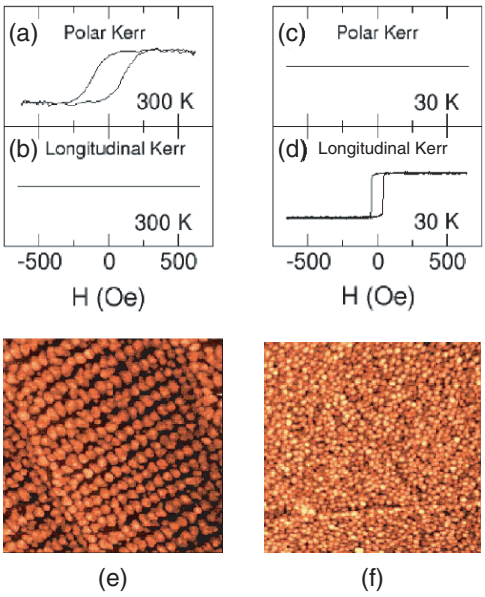

Figure 13. Kerr signal in the polar (H perpendicular to surface) and longitudinal (H parallel to surface) configuration for films of 1.7 ML of Co deposited at 300 K, (*a*) and (*b*); deposited at 30 K, (*c*) and (*d*). (*e*) Morphology of Co growth on Au(111) at 300 K, 1.0 ML (150 nm × 150 nm) and (*f*) at 30 K, 1.4 ML (100 nm × 100 nm). The 300 K growth leads to bilayer clusters 7 nm across while at 30 K a compact stacking of monolayer clusters with a diameter of 0.7 nm appears.

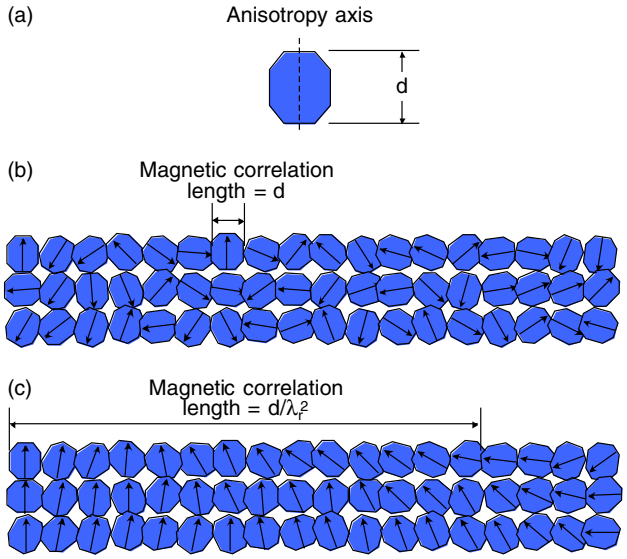

Figure 14. (*a*) Schematic representation of a magnetic nanoparticle with a uniaxial anisotropy axis (represented by a slight elongation); (*b*), (*c*) a stack of particles with randomly oriented anisotropy axes. In (*b*) $\lambda_r \geqslant 1$ and the magnetization vector points along the local anisotropy axis, so the magnetic correlation length is a single particle diameter. In (*c*) $\lambda_r < 1$ and the magnetic vectors are nearly aligned. The random perturbation from perfect alignment results in a finite magnetic correlation length that is a factor $1/\lambda_r^2$ larger than a single particle.

4.3. Pure cluster films

Beyond the percolation threshold, a cluster-assembled film becomes a single ferromagnetic infinite cluster with a complex morphology, and simple phenomenological models like the Curie–Weiss extension to the Langevin function (equation (6)) are not applicable. In this section we explore the behaviour of the extreme case, that is, a film of pure deposited clusters with no matrix. It is clear from looking at images such as the one shown in figure 3(*b*) that, although the film is ferromagnetic, the ground state configuration of spins will be different from that of a film made by depositing atoms. For example MFM images of cluster-assembled films do not show domains with clear boundaries in the conventional sense but a seemingly random patchwork arising from a continuously varying magnetic direction with a correlation length larger than a single deposited cluster [14] (see figure 16).

The previous section showed that the clusters and their anisotropy axes are randomly oriented in the assembly, so it is appropriate to apply a random-anisotropy (RA) model developed by several authors in the last two decades [39–43]. In this approach the magnetic ground state in a granular film is determined by the relative strength of a random anisotropy field

$$H_r = \frac{2K_r}{M_s} \tag{8}$$

and an exchange field

$$H_{ex} = \frac{2A}{M_s R_a^2}. \tag{9}$$

Here, K_r is the (randomly oriented) anisotropy of the grains, M_s is their saturation magnetization, A is the exchange constant for the interaction between the grains and R_a is the nanometre-scale region over which the local anisotropy axis is correlated, i.e. the characteristic grain size. The relative strength of the fields is given by the dimensionless parameter

$$\lambda_r = \frac{H_r}{H_{ex}}. \tag{10}$$

The model was originally developed to describe amorphous films in which a local, randomly-oriented, anisotropy is due to local atomic disorder. It is even better suited to providing a description of the magnetization in cluster-assembled films in which the distance R_a over which an anisotropy axis is correlated is well defined (i.e. the particle diameter). For $\lambda_r > 1$ the magnetic correlation length at zero field is R_a, and the magnetic vector in each particle points along the local intra-particle anisotropy axis ($b = 1$). Note that in an arrow representation this state would be identical to that in isolated non-interacting particles at absolute zero. With increasing inter-particle exchange (or decreasing intra-particle anisotropy) the configuration becomes a correlated super spin glass (CSSG) in which the magnetization vector in neighbouring particles is nearly aligned ($b \sim 0.5$), but the random deviation of the moments from perfect alignment produces a smooth rotation of the magnetization throughout the system with a magnetic correlation length, that is a factor $1/\lambda_r^2$, larger than the particle diameter. The difference between the two states is illustrated in figure 14.

The RA model has been used successfully to analyse the data in several *ex situ* magnetometry studies of cluster-assembled films [44–47] in which the films were capped by protective non-magnetic layers for removal from the deposition chamber. More recently a system developed to allow transfer

of a film directly into a vibrating sample magnetometer (VSM) in UHV conditions has enabled the study of exposed films without the protective non-magnetic capping layer [27, 28]. Here we present a case study of pure Fe and Co cluster films capped with Ag and analysed using the RA model. The particle sizes were the same as in the samples used to obtain isolated particle data shown in figure 5, that is, 3.0 nm and 2.8 nm diameter for the Fe and Co clusters, respectively. Thus the magnetic behaviour of the isolated and strongly interacting nanoparticles can be compared directly.

In a film whose ground state is a CSSG the RA model predicts an approach to magnetic saturation that depends on the dimensionality of the film [43]. In two dimensions the magnetization follows

$$M = M_s\left(1 - \frac{1}{32}\frac{\lambda_r^2}{\sqrt{h_{ex}}}\int_0^\infty dx C(x)x^2 K_1[x\sqrt{h_{ex}}]\right) \quad (11)$$

and in three-dimensions

$$M = M_s\left(1 - \frac{1}{30}\frac{\lambda_r^2}{\sqrt{h_{ex}}}\int_0^\infty dx C(x)x^2 \exp[x\sqrt{h_{ex}}]\right). \quad (12)$$

In equations (11) and (12), $h_{ex} = H/H_{ex}$, K_1 is the modified Hankel function and $C(x)$ is the correlation function for the anisotropy axes with x in units of R_a. In a cluster-assembled film with mono-sized clusters, $C(x)$ can be taken to be a simple step function with a cut-off at $x = 1$.

Figure 15 shows the approach to saturation for a 5 nm thick film of deposited Fe nanoparticles and a 20 nm thick film of deposited Co nanoparticles. The RA model curves were calculated using equation (11) for the Fe cluster film, which was only 2 cluster layers thick and equation (12) for the thicker Co cluster film. It is observed that in both cases the values of H_{ex} and H_r change little with temperature, which is just a confirmation of the observation that the shape of the curves appears to be independent of temperature. The value of the random anisotropy, K_r, obtained from H_r and equation (8) is shown in the insets and compared with the values for the isolated clusters. For the Fe cluster film, the random anisotropy is close to the isolated cluster value whereas for the Co cluster film it is significantly smaller. The exchange fields are ≈0.36 T and ≈0.6 T for the Fe and Co cluster films, respectively, corresponding to an exchange constant (from equation (9)) of $A \approx 3 \times 10^{-12}$ J m^{-1} for both films, which is much less than the bulk value as would be expected. Crudely one would expect a bulk-like exchange coupling only between atoms in contact at the interface between the particles; so averaged over the whole clusters, treated as 'giant atoms', it is much smaller. It appears from the value of A that about one atom in ten within the nanoparticle is exchange-coupled to atoms of neighbouring particles. For both the Fe and Co nanoparticle assemblies the exchange energy is about 170 meV per pair. This is similar to the value found in a two-dimensional assembly of Co nanoparticles on Si(001) prepared colloidally after removal of the ligand and oxide shells [48].

For both films the value of λ_r is close to 1, indicating that the magnetic configuration is close to the crossover between a simple spin glass, in which each cluster moment is aligned randomly in zero field, and the CSSG state. This crossover was directly observed in a 150 Å thick film of 3 nm diameter

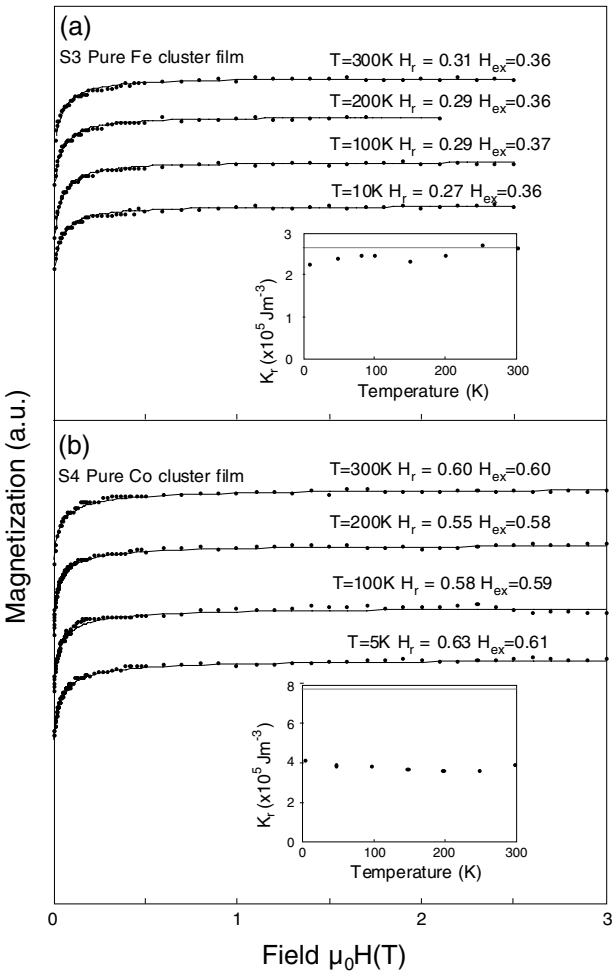

Figure 15. (*a*) Approach to the saturation of 5 nm thick pure Fe cluster (3.0 nm diameter) film for temperatures in the range 10–300 K (●) compared with a calculation using the RA model with the parameters shown (——). The inset shows the variation of the random anisotropy (evaluated from H_r and equation (8)) with temperature (●). The grey line shows the value for the isolated clusters. (*b*) As (*a*) but for the 20 nm thick pure Co cluster (2.8 nm diameter) film sample [27].

Fe nanoparticles [27]. The approach to saturation was fitted using the RA model as described above and it was found that with decreasing temperature the value of λ_r increased. For temperatures below 50 K it became greater than 1 and for the same temperature range the approach to saturation no longer followed the CSSG curve. This was attributed to a crossover from the CSSG to the simple spin glass configuration.

Recently the stray magnetic field at the surface of a pure Co cluster film was imaged using MFM [14]. Figure 16 shows the results for a 375 nm thick film produced by depositing 8 nm diameter Co nanoparticles, and it is observed that the stray field is a random patchwork as would be expected at the surface of a CSSG. By comparing directly the feature size in the MFM and the topographic image it was found that $\lambda_r \sim 0.67$, i.e. close to the value found in the Co cluster embedded film described above. In this particular study the Co particles had a thin native oxide layer producing a ferromagnetic/antiferromagnetic core–shell system with an exchange bias of 0.5 T at low temperatures after field-cooling

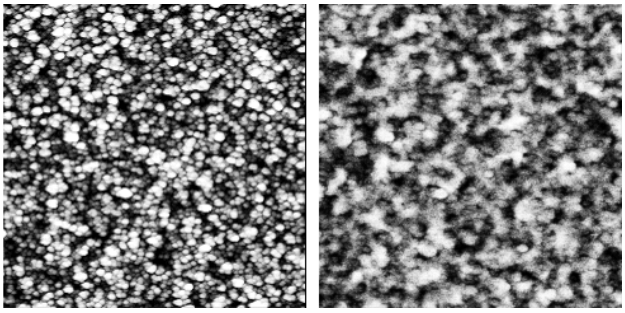

Figure 16. Topography and phase images of a 375 nm thick film of 8 nm diameter Co clusters deposited on Si(100). The scan size is 5000 nm [13].

(see section 7.3). The room temperature data however showed the soft magnetic behaviour characteristic of a CSSG, showing the formation of this state even in the case where the exchange interaction between the nanoparticles is complicated by an intervening antiferromagnetic layer.

Loffler *et al* [44, 45] also used the RA model to analyse magnetometry data from deposited gas-phase Fe and Ni nanoparticles with sizes in the range of 10–20 nm. They modified the deposited size distribution by post deposition annealing of the films [44] so that the study could be carried out as a function of particle size. The RA model produced good fits to the approach to saturation of the film magnetization, though in this case the fitted value of λ_r was 2. Although this is higher than the value at which a transition to a simple spin glass should occur, the critical value of λ_r is influenced by a number of factors including the distribution of anisotropy axes, which may not be truly random.

The same group used small angle neutron scattering to study the magnetic correlations in dense assemblies of Fe, Co and Ni nanoparticles deposited from the gas phase [45]. Again they annealed the samples to modify the average grain size *in situ* and discovered that the magnetic correlation length in Fe went through a minimum when the grain size equals the bulk domain wall width. They analysed their data using an extension of the RA model taking into account domain wall formation within grains. In fact even in the films composed of small (3 nm) nanoparticles described above, the assumption that the magnetization direction changes only at the interfaces (figure 14(*c*)) is an idealization and a more realistic model would have to include some curling of the magnetization within the grains.

Collecting all the results presented for the 3 nm Fe particles embedded in Ag the entire volume fraction range is qualitatively summarized in figure 17. Perfect superparamagnetism is observed only at very low volume fractions. For a large range of intermediate volume fractions the film can be considered to be exchange-coupled agglomerates of clusters (super-clusters) that interact with each other via dipolar forces. The magnetic behaviour in this region has been described as 'interacting superparamagnetism' [34] and can be modelled by a Curie–Weiss extension to the Langevin function describing perfect superparamagnetism. At the high volume fraction end the cluster films form a CSSG and show magnetically soft behaviour. At low temperatures and low volume fractions the system consists of isolated blocked

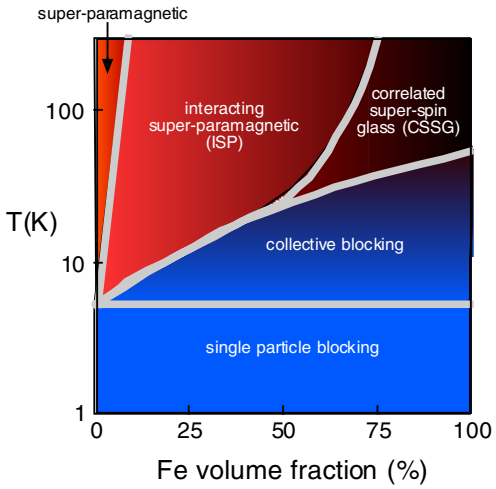

Figure 17. Magnetic phase diagram for films of deposited 3 nm diameter Fe nanoparticles embedded in Ag matrices as a function of volume fraction and temperature.

particles while at high volume fractions there is evidence that it forms a simple spin glass [27].

5. Magnetotransport in cluster-assembled films

Ever since the discovery, in 1992, of GMR in granular films consisting of magnetic nanoparticles in a non-magnetic matrix [49, 50] the origin of the effect has provoked much attention [51]. Although multilayer films in spin-valve structures have reached a very high level of performance in hard disk read heads, the GMR effect in nanogranular materials remains of interest both fundamentally and for high-field applications. Throughout this paper we have stressed the 'controllability' of the cluster/atom deposition technique both in terms of particle size and volume fraction; so it should be possible, using this method, to achieve a high GMR performance in terms of total resistance change between saturated and field-off states. The first measurement of GMR in a nanogranular material produced by depositing nanoclusters and a non-magnetic matrix was reported in 1997 [10].

A central issue in the production of granular films by cluster assembly is the effective size distribution of the embedded grains. Although the original clusters have a tight size distribution (even without mass selection) at the volume fractions required for high GMR performance, as shown in section 4.1, the magnetic grains consist of several of the deposited clusters exchange-coupled to behave, magnetically, as a single particle. It was also shown that the exchange-coupled aggregates interact via dipolar forces. In order to understand the variation of GMR with nanoparticle volume fraction it is useful to compare the experimental data with the MC model that was used to analyse the magnetization data from cluster-assembled films.

Figure 18 shows the relative resistance change versus applied field curves for two different volume fractions of Fe clusters embedded in Ag (circles). Also plotted are fitted curves using the model of Zhang and Levy (lines) [52] showing good agreement for volume fractions up to the percolation threshold. The increasing GMR with volume fraction is

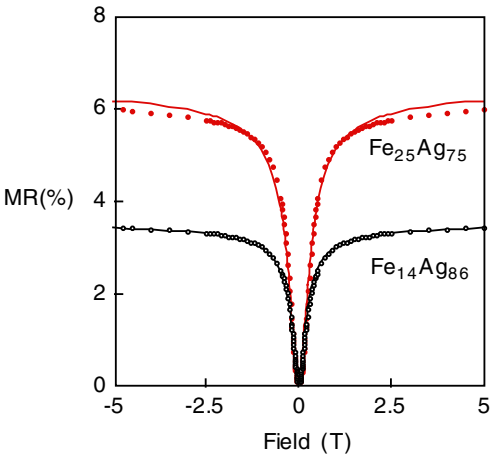

Figure 18. Resistance change (defined by $[R(H) - R(0)]/R(0)$ max) at room temperature for Fe clusters embedded in Ag at two different volume fractions (circles). The lines are fits using the model of Zhang and Levy [48].

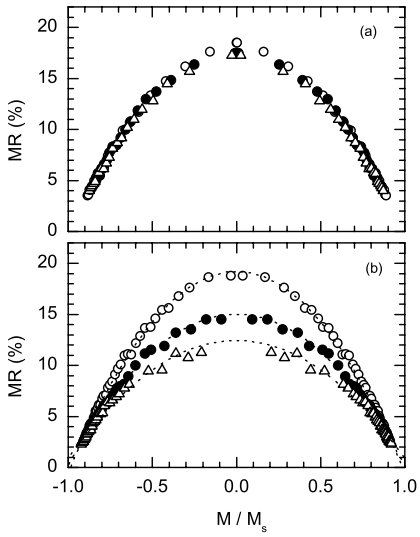

Figure 19. GMR versus sample magnetization for (*a*) a monodisperse sample and (*b*) a polydisperse sample. For both samples the volume fraction is 25%. Open circles are non-interacting anisotropic clusters, closed circles are interacting anisotropic clusters and triangles are interacting isotropic clusters. The dotted lines are fitted parabolas.

evident in the figure but if the volume fraction is pushed higher the magnitude of the GMR decreases again.

Even without inter-particle interactions the GMR amplitude is expected to decrease at volume fractions above the percolation threshold as the clusters form a continuous network. The optimum volume fraction has been shown to be a result of the competition between the increasing number of magnetic centres that enhance the effect and the increase of the average grain size that suppresses it [53]. There is an additional reduction due to inter-particle interactions as is evident from the MC model. Figure 19 shows that including the inter-particle dipolar interaction produces a suppression of the peak GMR response as a result of an increasing magnetic alignment. The difference in spin-dependent valence electron scattering between the field on and field off states required for GMR is thus reduced.

The occurrence of an optimum volume fraction for GMR performance is demonstrated clearly in figure 20(*a*) showing the maximum relative resistance change measured as a function of volume fraction for Fe and Co clusters embedded in Ag. In both cases there is an optimum value, but this is higher in the case of Co clusters. From the previous discussion the reason for this can be identified. As shown in section 3.1, Co clusters embedded in Ag have a much higher anisotropy than Fe clusters. This increased anisotropy maintains the magnetization of the Co clusters along the (randomly oriented) local anisotropy axis against a stronger dipolar interaction between the clusters. This remains true when the relevant magnetic particles are exchange-coupled agglomerates of the deposited Co clusters. The dipolar interaction between Co particles (isolated clusters or agglomerates) is also weaker than between Fe clusters due to their lower spin moment. Thus the Co clusters can be packed to a higher density before the dipolar interactions start to degrade GMR performance. This shifts the GMR peak to a higher volume fraction and thus also to a higher value. This behaviour is reproduced by the MC model as shown in figure 20(*b*) for interacting and non-interacting clusters, which, in the limit, can be taken to represent the case of Fe and Co clusters. However, the model predicts a higher resistance change than is observed.

6. High moment soft films

The possibility of producing materials whose magnetization exceeds the SP limit of 2.45 T (in $Fe_{70}Co_{30}$ alloy) by using cluster assembly was first suggested by measurements of enhanced magnetic moments in free Fe, Co and Ni clusters containing less than 600 atoms [54]. A few years later, measurements of the orbital and spin moments in size-selected nanoparticles using XMCD [55] showed that small supported (but isolated) clusters maintain a higher magnetization than the bulk and about half of this enhancement comes from a large increase in the orbital moment. It was quickly realized, however, that simply depositing Fe particles on a surface would not produce a high-moment film, since when the particles come into contact the orbital moment reverts to its small bulk value [36]. More significantly depositing nanoparticles with no matrix produces a very porous film with about 50% of the bulk density [56], so enhanced magnetization in the clusters will not translate into a large generated magnetic field.

More recently an XMCD measurement of the orbital and spin moments in supported Fe nanoparticles after they had been coated *in situ* with Co revealed that the coating enhanced the spin moment still further but did not significantly reduce the orbital contribution [57]. This led to the suggestion that depositing Fe nanoparticles in conjunction with Co atoms as in figure 1 is a possible route to producing high-moment films [12]. As shown in section 4.2 the nanogranular structure with randomized anisotropy in the films will automatically produce soft magnetic behaviour.

Verifying this possibility using size-selected nanoparticles is far from trivial. To begin with XMCD measurements can be performed on tiny amounts of material (~0.1 Å equivalent film thicknesses), and so depositing a suitable sample with tight mass selection is no problem. To produce enough material using size-selected clusters to get an accurate moment determination using a conventional magnetometer such as a

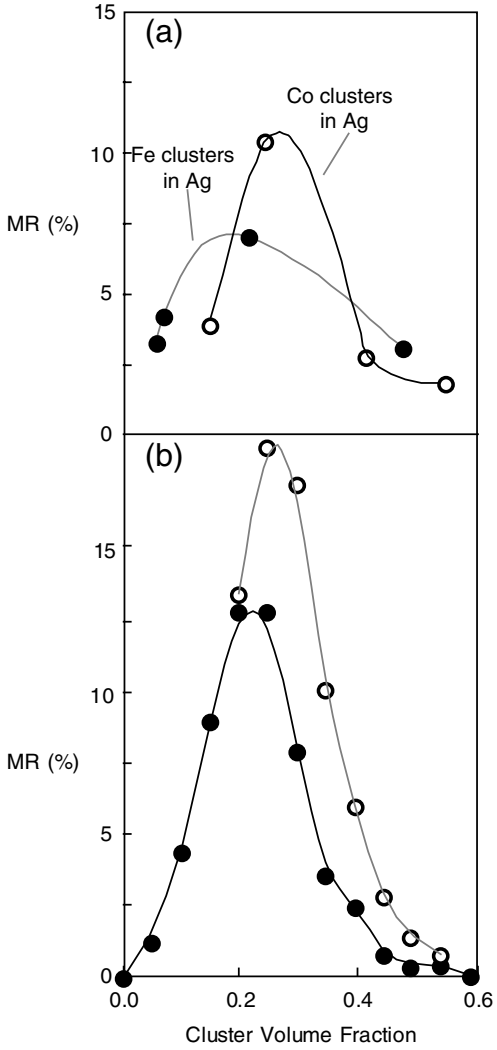

Figure 20. (*a*) Resistance change (defined by $[R(H) - R(0)]/R(0)$ max) at 2 K versus volume fraction for Fe clusters in Ag (●) and Co clusters in Ag (○). (*b*) Dependence of GMR on magnetic particle concentration predicted by the MC model. Open circles are non-interacting anisotropic clusters and closed circles are interacting anisotropic clusters. The percolation threshold is at a volume fraction of 0.3.

VSM requires very long deposition times with normal cluster sources. Using a much more sensitive SQUID magnetometer is not helpful since this also amplifies the substrate (background) signal. To get a high precision measurement requires enough magnetic material to produce a bigger ferromagnetic signal than the diamagnetic or paramagnetic background from the substrate, which in practice means a film ∼500 Å thick. The other technical problem is that there is no reliable high precision measurement of the amount of material deposited in a thin film.

In a recent study [58] the technical hurdles were overcome by using aerodynamic lensing [59] to produce a high flux of particles of about the right size and producing large numbers of samples so that averaging could be carried out. The amount of material in the samples was determined by calibrating a quartz oscillator thickness monitor using the magnetic signal in a VSM. Figure 21 shows the measured magnetization per atom as a function of volume fraction for Fe nanoparticles containing

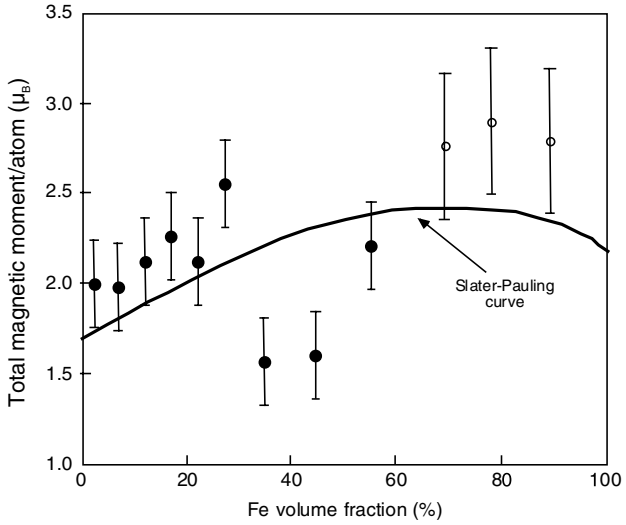

Figure 21. Magnetic moment per atom in films of Fe clusters (mean size 150 atoms) embedded in Co matrices as a function of Fe volume fraction. The amount of Fe was determined using a quartz oscillator calibrated using pure Fe and pure Co films (●). The black line is the SP curve for conventional FeCo alloys. The open circles show some measured values obtained by swapping materials, i.e. Co clusters embedded in Fe matrices.

about 150 atoms in a Co matrix (filled circles). The SP curve for homogeneous Fe–Co alloys is shown for comparison. It is clear that at low Fe volume fractions the cluster-assembled film has a higher magnetization per atom but at the percolation threshold a drastic reduction to well below the SP curve occurs. This is predictable since above the percolation threshold the film can be considered to be a phase-separated mixture of Fe and Co, so the moment will be a weighted average of the bulk Fe and Co values.

In a film with densely packed nanoparticles, the matrix itself will be in a nanogranular form and so in principle one can make the nanogranular Fe–Co by having either material deposited as nanoparticles. If the materials are swapped, that is Co nanoparticles are embedded in an Fe matrix, (open circles in figure 21) the high Fe volume fraction end of the granular mixture can be investigated. The measured magnetization at this end of the curve could well exceed the SP maximum but the large error bars prevent a confident assertion of this point. In addition even embedded cluster films will probably not achieve 100% of the bulk density and the actual porosity of the embedded cluster films is not known. In section 2.2 it was shown that Co clusters in Fe matrices have the bcc structure and the more open atomic structure may well produce an extra enhancement in the magnetization of the Co nanoparticles. A recent tight-binding calculation (table 5) of core–shell FeCo nanoparticles with a bcc structure containing 339 atoms in the core and 302 atoms (2 monolayers) in the shell indicates that the moment is higher if the Co is the core material [60].

7. Binary clusters

The previous sections of the review have demonstrated the high degree of flexibility in the properties of magnetic materials produced by cluster assembly. In this final section we turn to yet another parameter allowing further control, that

Table 5. Calculated moments of Co clusters in Fe shells and vice versa.

Cluster	Co M_l (μ_B)	Co M_s (μ_B)	Co M_{tot} (μ_B)	Fe M_l (μ_B)	Fe M_s (μ_B)	Fe M_{tot} (μ_B)	Average μ/atom (μ_B)
$Co_{339}Fe_{302}$	0.13	1.74	1.87	0.13	2.74	2.87	2.34
$Fe_{339}Co_{302}$	0.22	1.79	2.01	0.10	2.38	2.48	2.26

is, production of nanoparticles made out of more than one element, which is increasingly the focus of cluster studies. Two different classes of binary clusters specialized to different tasks will be described, that is, high-moment mixtures such as Fe–Co and high anisotropy mixtures, that is, CoSm, FePt and CoRh.

7.1. High-moment FeCo nanoparticles

An alternative approach to producing high moment films by assembling nanoclusters is to make the clusters themselves as binary Fe–Co particles. These were successfully produced at the University of Rostock by an arc cluster ion source (ACIS) employing an FeCo alloy target [61]. XMCD was used to measure the orbital and spin moments localized on the Fe and Co atoms in mass-filtered Fe–Co clusters with a mean size of about 7.5 nm deposited *in situ* onto ferromagnetic Ni(111) films on a W(110) crystal in UHV. The data were recorded in remanence after magnetization with an external magnet, and since the Ni films have a remanence that is nearly 100% of saturation the exchange coupling with the Fe–Co clusters at the surface ensures that the clusters were saturated, as required for a sum rule analysis of the magnetic moments. Figure 22 shows the photoabsorption spectra of the two metals involved, Fe and Co. It is seen that the dichroism has the same sign for the spectra demonstrating the ferromagnetic coupling between the elements. The figure also illustrates nicely the element sensitivity of the technique that yields, independently, the magnetic moment of each metal.

A sum rule analysis of the optical absorption data reveals enhanced spin and orbital moments in both constituents (Fe and Co). These are listed in table 6 and compared with the bulk values. The Fe moments in the alloy particles agree with calculated values for the $Fe_{50}Co_{50}$ bulk [62] whereas the Co moments exceed the calculated values by about 15% (spin moment) and 50% for the orbital moment. Note that the estimated uncertainty in the experimental values is about 10%.

The increased magnetic moment in bulk Fe–Co alloys can be understood by the increased spin polarization due to the degree of band filling within a rigid band model. When assuming a homogeneous mixture of Fe and Co in these relatively large particles (∼7.5 nm diameter), it is likely that the behaviour is similar to the bulk. However, even for a 7.5 nm particle, an additional perturbation arises due to the fact that ∼40% of the atoms are on the two outermost surface atomic layers in which increased orbital moments are expected. Although it is known that calculations in general underestimate the orbital moment, the data indicate that there is some additional enhancement arising from the high surface to volume fraction in nanoparticles. Such an enhancement in the orbital moment has been found also in large Fe nanoparticles with sizes up to 12 nm [61].

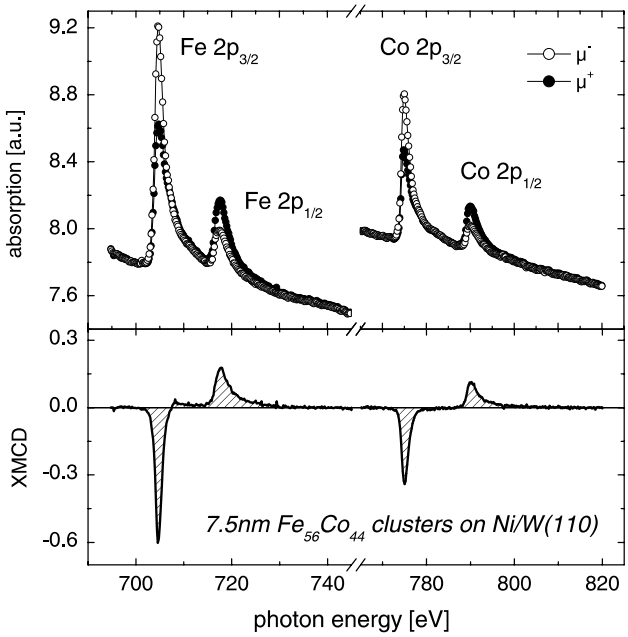

Figure 22. Upper part: photoabsorption spectra of 7.5 nm Fe–Co particles deposited on an Ni(111) film on W(110) taken in remanence with circularly polarized radiation for opposite magnetization directions μ^+ and μ^-. Lower part: corresponding XMCD data (intensity differences).

As the particles get smaller, the bulk interpretation becomes less applicable. Recent *ab initio* theoretical studies of very small Fe_mCo_n clusters, where $m + n \leqslant 6$ [64] and $m+n = 5, 13$ [65], showed that the moment per atom increases monotonically as a function of the Fe content rather than going through a peak as observed in the SP curve. It was also shown in the case of 5-atom Fe_mCo_n [64] clusters that the moment is enhanced relative to pure Fe clusters of the same size due to structural changes induced by including Co.

7.2. High anisotropy nanoparticles

7.2.1. SmCo. The high coercivity of the bulk $SmCo_5$ alloy suggests the possibility of producing small (<5 nm) nanoparticles of SmCo that are magnetically blocked at room temperature and thus capable of storing a data bit. Nanoparticles of SmCo with a mean diameter of 3.5 nm were successfully produced at the University of Lyon by a laser ablation cluster source using a $SmCo_5$ target rod, and subsequent RBS analysis of samples showed a Co/Sm ratio of 4.8 [66]. High-resolution TEM images showed that the as-deposited clusters were amorphous but post-deposition annealing at 570 °C produced an improved crystallinity. The perfect hexagonal structure of the bulk $SmCo_5$ phase was, however, never observed. X-ray photoelectron spectroscopy

Table 6. Magnetic moments of pure Fe, Co and of 7.5 nm $Fe_{56}Co_{44}$ alloy clusters deposited onto Ni/W(110) [61]. The corresponding bulk values have been taken from [63].

	Co M_l (μ_B)	Co M_s (μ_B)	Co M_{tot} (μ_B)	Fe M_l (μ_B)	Fe M_s (μ_B)	Fe M_{tot} (μ_B)	Average μ/atom (μ_B)
Fe_{56} Co_{44}	0.21	2.00	2.21	0.10	2.30	2.40	2.32
Fe, Co bulk	0.15	1.55	1.70	0.09	2.00	2.09	—

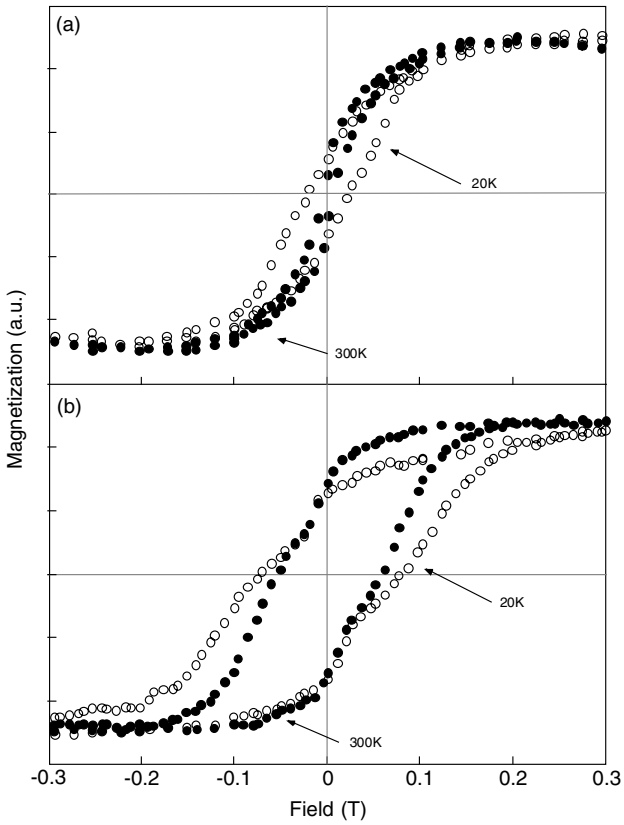

Figure 23. VSM-measurements performed at 20 K (○) and room temperature (●) on films of 3% $SmCo_5$ nanoparticles embedded in niobium, deposited on sapphire substrates at room temperature. (*a*) As-deposited film and (*b*) after annealing for 30 min at 570 °C.

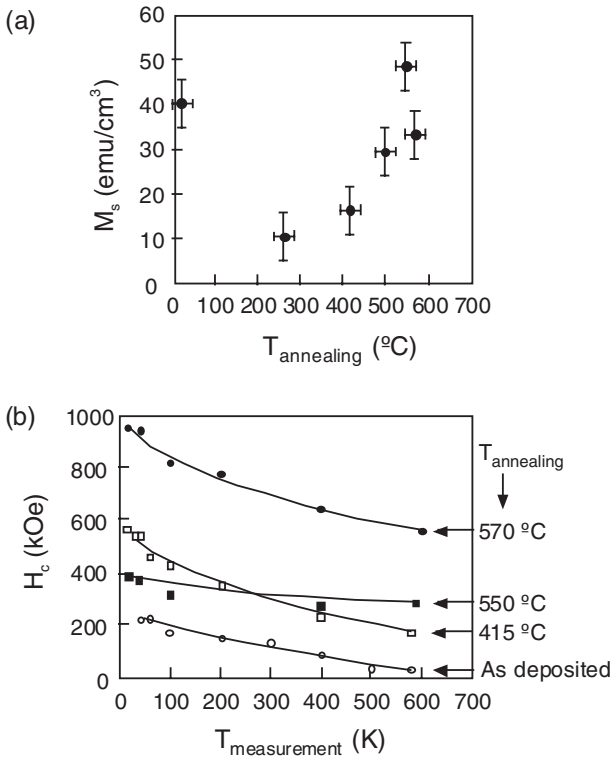

Figure 24. (*a*) Evolution of the saturation magnetization M_s as a function of the temperature of the post annealing treatment of the CoSm /Nb films. (*b*) Evolution of the coercive field H_c in the temperature range 10–300 K in CoSm/Nb films as deposited and films subsequently annealed at temperatures up to 570 °C.

of the deposited clusters showed that the Sm atoms were segregated on the cluster surface.

The magnetization measurements were carried out with a VSM on samples of clusters embedded in a Nb matrix, which is immiscible with the Sm shell, with a volume fraction of 3% at which the cluster–cluster interactions can be neglected. Figure 23 shows the hysteresis for the as-deposited films (figure 23(*a*)) and after annealing *in situ* in UHV at 570 °C (figure 23(*b*)). A relatively low saturation magnetization ($M_s \approx 15$ emu cm^{-3}) and low coercive field are seen in the as-deposited films, the latter resulting in a blocking temperature T_b lower than room temperature. After annealing up to 570 °C, when the clusters are recrystallized (figure 23(*b*)), the saturation magnetization, M_s, at 20 K increases up to 50 emu cm^{-3} (figure 24(*a*)). At the same time, the coercive field H_c increases up to 0.080 T at 20 K and 0.057 T at room temperature (figure 24(*b*)). The improved magnetic parameters, which are a result of the atomic rearrangements in the clusters upon annealing, are still much less that those of the bulk crystalline $SmCo_5$ phase [67]. It is well known that defects in the nominal stoichiometry or an imperfect crystallinity lead to reduced M_s and H_c values. This early attempt to use binary clusters is, however, promising especially in terms of magnetic anisotropy, since the blocking temperature T_b of isolated mixed Co–Sm nanoclusters after annealling is above room temperature, which is exceptional for such small magnetic particles. For comparison, the blocking temperature of pure Co-clusters in the same size-range is around 20–30 K.

7.2.2. CoPt. The Lyon group also produced well-crystallized CoPt nanograins with a mean diameter of about 2 nm [68]. In this case hybridization between the 3d Co and the 5d Pt orbitals is expected to produce an increase in the magnetic anisotropy. Various compositions of target rod were used and the compositions of the binary clusters were found to be close to those of the targets with a slight enrichment in Co and an atomic structure dependent on composition. $Co_{0.75}Pt_{0.25}$ binary clusters exhibited the $L1_0$ tetrahedral–crystalline structure while the measured global composition

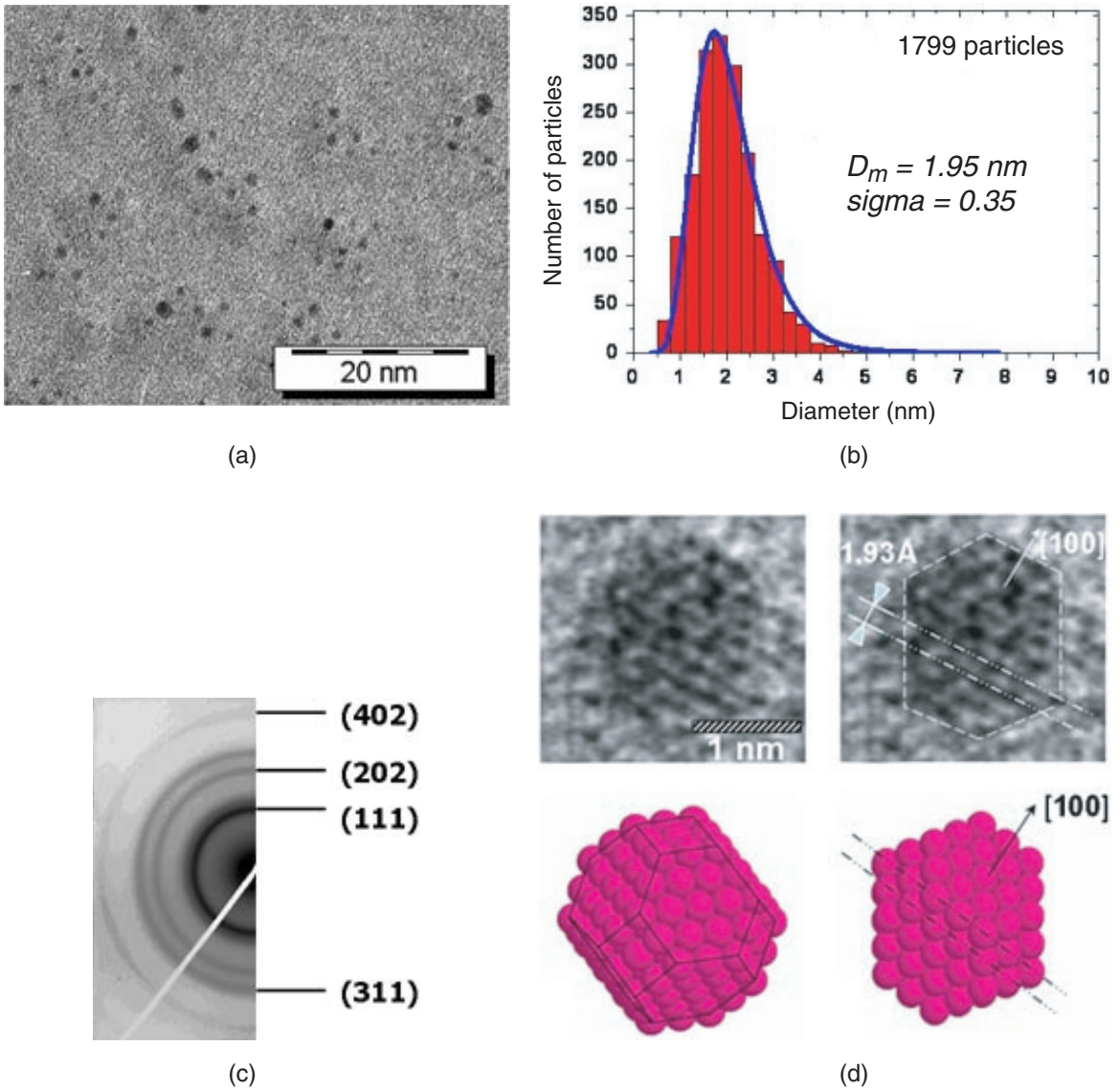

Figure 25. (*a*) TEM-image of isolated $Co_{0.58}Pt_{0.42}$ binary clusters deposited on an amorphous-carbon coated grid at room temperature. (*b*) The corresponding size-histogram. The solid line in (*b*) corresponds to the fitted distribution using a log–normal shape. The mean diameter of the clusters, D_m, and standard deviation sigma deduced from this fitted distribution are directly indicated in the figure. (*c*) The disordered-alloy phase (cubic A1-phase) is shown by the electron diffraction pattern. (*d*) HRTEM-images of some selected clusters with the corresponding simulations.

of the nanograins ($Co_{0.82}Pt_{0.18}$) was not the one corresponding to this ordered alloy ($Co_{0.50}Pt_{0.50}$) in the phase diagram of the Co–Pt system. This can be explained by a non-homogeneous distribution of atoms leading to cluster cores with the correct composition to form the $L1_0$ phase surrounded by a Co-rich shell. With increased Pt-content in the target rod ($Co_{0.50}Pt_{0.50}$) to produce $Co_{0.58}Pt_{0.42}$ clusters, the fcc A1-phase is observed (figure 25). This disordered alloy-phase is present in the phase diagram of the Co–Pt system at high temperatures. The cubic symmetry of this phase is expected to produce a lower magnetocrystalline anisotropy than the tetrahedral symmetry of the $L1_0$ phase. Increasing the Pt content further by using a $Co_{0.25}Pt_{0.75}$ target, the fcc-crystalline Pt-phase is observed indicating a complete segregation of both species in these clusters.

SQUID measurements performed on the $Co_{0.58}Pt_{0.42}$ clusters embedded in Nb at low volume fractions reveal a significant increase of the blocking temperature, T_b, up to 50 K (figure 26), compared with the T_b value of about 12 K previously measured for pure Co clusters with the same size embedded in a Nb matrix [68]. The number of Co atoms in the $Co_{0.58}Pt_{0.42}$ binary clusters is however of the order of 300 compared with about 1000 per pure Co-cluster with the same size (fcc-truncated octahedron). This emphasizes the important role of Pt atoms in increasing the magnetic anisotropy and thus the blocking temperature despite not having the optimum atomic structure.

7.2.3. CoRh. Theoretical studies of several 3d–4d and 3d–5d clusters have been performed in order to quantify the dependence of the magnetic moments, magnetic order and magnetic anisotropy energy (MAE) on the relevant parameters [69]. Here we focus on calculations for Co_nRh_m, to highlight

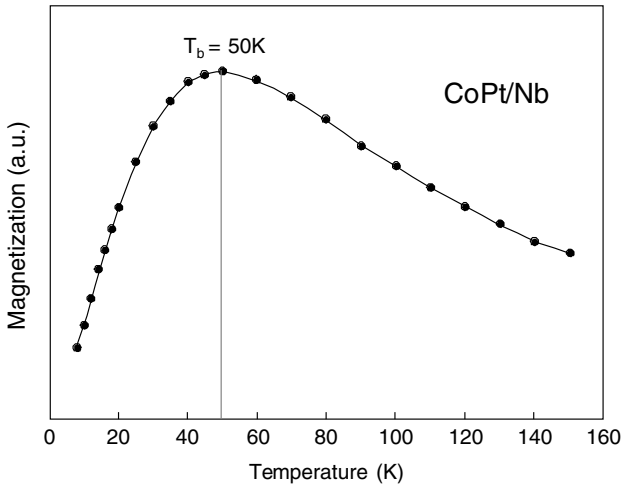

Figure 26. ZFC-magnetization curve measured from isolated $Co_{0.58}Pt_{0.42}$ binary-clusters with a 10 mT applied magnetic field. The cluster volume fraction (<5%) was sufficiently low to neglect coalescence of clusters.

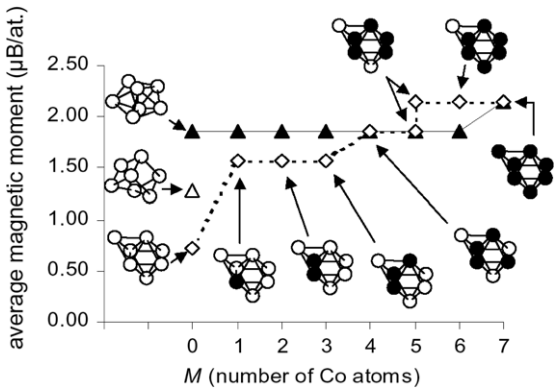

Figure 27. Average magnetic moments in seven-atom Co_MRh_N clusters as a function of the number of Co atoms (●) [72].

the role of the 3d–4d interaction in increasing anisotropy. The dominant contribution to the MAE of small particles is the spin–orbit (SO) interaction, which is very sensitive to the details of the spin-polarized density distribution and of the electronic spectrum. In binary 3d–4d clusters the electronic states are metallic-like, i.e. delocalized throughout the particle [70, 71]; however calculation methods enable the description of the magnetic properties of each individual 3d and 4d atom and to analyse their dependence on the local environment. Such a local analysis has been shown to be a powerful tool in correlating the magnetization and anisotropy of the particles with the microscopic parameters that can be tuned in experiment (e.g. composition, structure, etc) [72–75].

The 4d atoms play a very important role in the MAE of binary clusters and nanostructures. Very often it is the 4d part of the MAE at the interfaces that determines the orientation of the easy axis and the absolute value of the energy barrier. In fact, most remarkable behaviour of 3d–4d systems, such as enhanced MAE and perpendicular or canted easy axes, is found when the 4d contributions dominate. For example, in the case of Co clusters deposited on Pd surfaces, it has been shown that the perpendicular easy axis is a consequence of the induced moments and the resulting SO coupling at the Pd atoms of the interfaces [73–75].

The SO interactions responsible for the MAE are most effective near the nuclei. Therefore, they are intimately related to the existence of local spin moments at the d orbitals of each individual atom. A necessary condition for maximizing the 4d contributions to the MAE is the development of significant spin moments at the 4d atoms. The role of the stronger SO coupling at 4d elements in a 3d–4d cluster is not to enhance the SO energy associated to the magnetic moments of the 3d atoms (e.g. by some sort of SO proximity effect) but rather to yield an important effect when the 4d orbitals are spin polarized. Thus the local magnetic moments of the 4d atoms and their order are crucial for the magnetoanisotropic behaviour of 3d–4d nanostructures. The calculations explicitly show that neglecting the 4d contributions completely changes the magnetoanisotropic properties [73–75]. In the case of Co_nRh_m clusters one observes that the Co atoms preserve high magnetic moments, which are of the order of the bulk Co local moment or even larger if they occupy a weakly coordinated surface site [76–78]. This is so even in very rich 4d environments. Simultaneously, the Rh, Pd or Pt atoms close to Co develop local spin moments by proximity effects which increase with increasing number of Co atoms in their NN shells. Therefore, intermixing at interfaces usually enhances the 4d spin moments and the 4d contributions to the MAE [79].

Different size regimes must be distinguished concerning the ability of a 4d cluster (e.g. Rh_n) to increase its magnetic moment as a result of alloying with a 3d element (e.g. Co). For very small sizes, Rh_n is in general already magnetic on its own ($n < 10$), and the possibility of a further increase of the Rh moments is relatively small (see figure 27). Co substitution yields an increase of the cluster magnetization, which is basically due to the larger local moments at Co atoms [78]. As the size increases there is a transition from ferromagnetic (FM) to paramagnetic (PM) behaviour, which in Rh_n occurs for $n \approx 50$ atoms. In this case the effects of 3d alloying are dramatic; for example, calculations have shown that replacing just one Rh atom by a Co in Rh_{38} induces an increase of $16\mu_B$ in the total magnetization [80]. This also results in a large increase of the MAE. Finally, in the technologically most interesting nanoparticle regime (above hundreds of atoms) the 4d magnetism and the associated MAEs can only survive close to the 3d–4d interfaces [81]. The shape and structure of these interfaces and their possible interaction with the cluster surface become crucial for the magnetic behaviour.

In order to illustrate how the distributions of 3d and 4d atoms within a nanoparticle condition the magnetic behaviour, consider a Co_xRh_{1-x} cluster having $n \approx 400$–500 atoms and $x \approx 0.5$. If one assumes a segregated core–shell structure with a Co core coated by a number of Rh shells, the average magnetization of the clusters is small (typically $1.27\mu_B$ per Co atom), the Co moments are similar to the bulk moment and the induced moments at the Rh atoms are small (about $0.05\mu_B$) and localized at the Co–Rh interface. The resulting MAE corresponds approximately to that of pure Co_n. This can be explained by observing that the Co atoms have bulk-like coordination (with some of its neighbours being weakly magnetic Rh atoms) and that the curvature of the

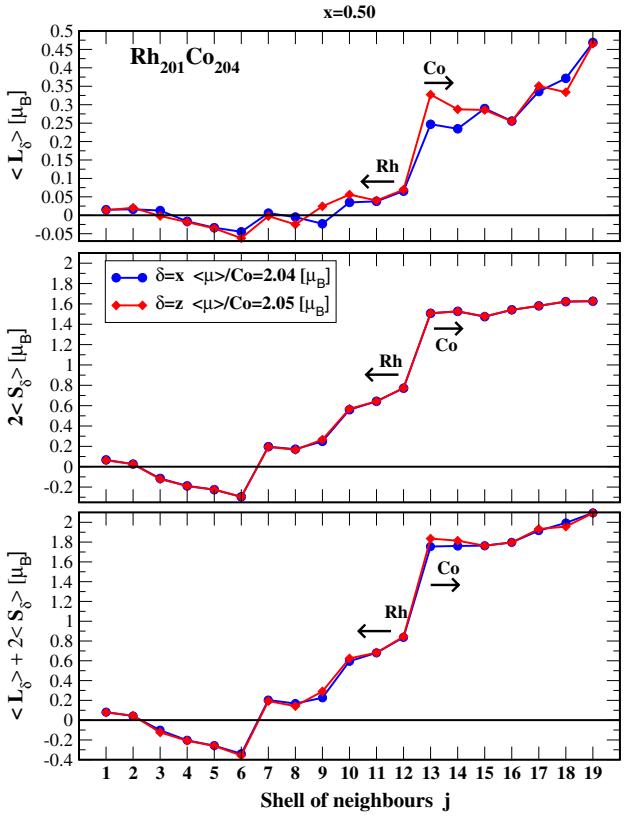

Figure 28. Local magnetic moments in fcc-like $Rh_{201}Co_{204}$: orbital contribution $\langle L_j \rangle$, spin contribution $\langle 2S_j \rangle$ and total moment $\langle M_j \rangle = \langle 2S_j \rangle + \langle L_j \rangle$. The cluster is formed by a Rh core surrounded by surface Co shells and a sharp interface [73, 74].

Rh surface is large for such sizes. Therefore the surface Rh atoms, which have no Co neighbours, remain weakly magnetic or non-magnetic as in the bulk. In the opposite segregated configuration (Rh core and Co surface) the situation changes qualitatively. The Co atoms at the surface show enhanced magnetic moments (about $2.0\mu_B$) basically like in a pure Co cluster; the Co–Rh interface has a small curvature, with the Rh atoms having many Co neighbours and thus developing significant magnetic moments (about $0.6–1.2\mu_B$, see figure 28). In this way both the magnetization and the MAE are significantly enhanced. Similar trends are expected for other 4d elements.

7.3. Core–shell metal–oxide nanoparticles

An alternative to incorporating two metals into clusters is to produce core–shell nanoparticles by a controlled oxidation of a pure metal core. This can be achieved either by introducing oxygen into the carrier or sputtering gas of a cluster source or by a controlled dosing of pre-formed pure metal nanoparticles [7, 83, 84]. In materials where the metal oxide is antiferromagnetic (e.g. CoO) this introduces the possibility of an exchange bias 'built-in' to each particle, though whether this really happens in isolated particles in which there is only one or two atomic layers in the oxide shell is debatable. In small core–shell nanoparticles inter-particle interactions may be required to produce a stable Neel vector in the antiferromagnetic regions of the sample. Exchange bias was originally detected some time ago in (large) oxidized Co particles by MeikleJohn and Bean [82], and the advent of cluster sources able to produce small size selected core–shell clusters has added a new impetus for studying particles. Systems containing a ferromagnetic/antiferromagnetic interface generally develop a unidirectional anisotropy or exchange bias if they are field-cooled through the Neel temperature of the antiferromagnet. This is easy to understand in the case of a layered antiferromagnet where the layers are parallel to the interface. Application of an external field to the system does not affect the Neel vector, but the ferromagnetic region of the sample has an additional exchange field to overcome at the interface in one direction. The effect, however, is also observed in more complex spin configurations. Below we present two case studies.

7.3.1. Co–CoO. Peng *et al* [6] developed the technique for oxidizing gas-phase nanoparticles within their cluster source and carried out a magnetometry study of monodispersed Co–CoO core–shell particles deposited on polyimide substrates. By changing conditions in the source it was possible to produce depositions of particles with (total) diameters of 6 and 13 nm. TEM showed the coexistence of fcc Co and CoO phases, and high resolution imaging confirmed the existence of the oxide phase in a shell around a metallic core and showed that the shell itself was composed of very small crystallites [83]. The existence of a single antiferromagnetic oxide phase in the shell makes this a model core–shell ferromagnetic–antiferromagnetic system.

It was found that the exchange bias increases and stabilizes with the level of oxygen exposure within the source indicating that the oxide shell thickness grows with dose but then stabilizes at some thickness. At no dose was there a complete conversion of the particles to pure CoO. It was found that the smaller (6 nm) particles exhibited the largest exchange bias, which reached a value of 1.02 T at 5 K, compared with 0.36 T for the 13 nm particles. This was attributed to the higher proportion of atoms at an interface in the smaller particles. With increasing temperature the exchange bias decreased and vanished at about 200 K, which is much less than the bulk CoO Neel temperature of 293 K. The reduced temperature was attributed to spin disorder around the core–shell interface.

7.3.2. Fe–Fe oxide. Fauthe *et al* and Kuhn *et al* [7, 84] developed a similar process for producing an oxide shell on gas-phase Fe nanoparticles though in this case the oxide formed was a mixture of Fe_3O_4 and Fe_2O_3 phases [84], each with a different spin configuration, making it a much more complicated system than Co–CoO. The particles were in the size range of 5–25 nm and it was found that the oxide shell formed with a stable thickness of 3 nm and was resistant to further oxidation. A synchrotron radiation study using XMCD was carried out on particles deposited on GaAs substrates at low coverage [7] in which the x-ray absorption was measured using both total electron yield (TEY) and fluorescence yield (FY). These detection techniques probe different depths of the sample with the TEY signal coming from the uppermost few nanometres, that is, about the thickness of the oxide shell. Thus the oxide signal is greatly enhanced in the TEY spectra, compared with those measured using FY. The authors used

this contrast to show a gradient in the oxide stoichiometry that changes from an Fe_3O_4 layer at the metal oxide interface to a Fe_2O_3 layer at the particle surface. The study also demonstrated a strong ferromagnetic coupling between the core and the oxide shell and a zero magnetization with no applied field that was attributed to a strong spin canting throughout the particles.

8. Conclusions

We have described the structure and magnetic properties of pre-formed gas-phase magnetic nanoparticle deposited on surfaces and embedded in matrices by co-deposition with an atomic vapour. We have shown that magnetic thin films produced this way have very flexible properties and by varying the size and volume fraction of the nanoparticles, which can be done independently, it is possible to exercise a great deal of control over the magnetization behaviour of the materials. This flexibility coupled with the ability to produce nanogranular mixtures of miscible metals could lead to new high-performance materials such as soft magnetic films whose magnetization exceeds the SP limit. We have also described recent progress in producing bi-metallic gas-phase magnetic nanoparticles adding a further dimension of flexibility to the design of nanostructured magnetic materials produced by cluster deposition.

Acknowledgments

We would like to acknowledge support from EC contract No G5RD-CT-2001-00478 (AMMARE) and the hard work of Professor Antonis Andriotis, IESL, FORTH, Crete, who co-ordinated the AMMARE project.

References

[1] Echt O, Sattler K and Recknagel E 1981 *Phys. Rev. Lett*. **11** 1121–4
[2] Knight W D, Clemenger K, de Heer W A, Saunders W A, Chou M Y and Cohen M L 1984 *Phys. Rev. Lett.* **52** 2141–3
[3] Pedersen J, Bjørnholm S, Borggreen J, Hansen K, Martin T P and Rasmussen H D 1991 *Nature* **35 3** 733–5
[4] Balian R and Bloch C 1972 *Ann. Phys. NY* **69** 76
[5] Perez A *et al* 1997 *J. Phys. D: Appl. Phys.* **30** 709–21
[6] Peng D L, Sumiyama K, Hihara T, Yamamuro S and Konno T J 2000 *Phys. Rev.* B **61** 3103–9
[7] Fauth K, Goering E, Schutz G and Kuhn L T 2004 *J. Appl. Phys.* **96** 399–403
[8] Kholmanov I N, Barborini E, Vinati S, Piseri P, Podesta A, Ducati C, Lenardi C and Milani P 2003 *Nanotechnology* **14** 1168–73
[9] Perez A, Bardotti L, Prevel B, Jensen P, Treilleux M, Melinon P, Gierak J, Faini G and Mailly D 2002 *New J. Phys.* **4** 76
[10] Parent F *et al* 1997 *Phys. Rev.* B **55** 3683–7
[11] Binns C, Edmonds K W, Baker S H, Maher M J, Thornton S C and Upward M D 2001 *Scr. Mater*. **44** 1303–7
[12] Binns C, Louch S, Baker S H, Edmonds K W, Maher M J and Thornton S C 2002 *IEEE Trans. Magn.* **38** 141–5
[13] Qiu J M, Xu Y H, Judy J H and Wang J P 2005 *J. Appl. Phys.* **97** 10P704
[14] Koch S A, Palasantzas G, Vystavel T, De Hosson Th M, Binns C and Louch S 2005 *Phys. Rev.* B **71** 085410
[15] Haberland H, Insepov Z and Moseler M 1995 *Phys. Rev.* B **51** 11061–7
[16] Vandamme N, Janssens E, Vanhoutte F, Lievens P and Van Haesendonck C 2003 *J. Phys.: Condens. Matter.* **15** S2983–99
[17] Bardotti L, Prével B, Mélinon P, Perez A, Hou Q and Hou M 2000 *Phys. Rev.* B **62** 2835–42
[18] Bardotti L, Prevel B, Treilleux M, Melinon P and Perez A 2000 *Appl. Surf. Sci.* **164** 52–9
[19] Yoon B, Akulin V M, Cahuzac Ph, Carlier F, De Frutos M, Masson A, Mory C, Colliex C and Bréchignac C 1999 *Surf. Sci.* **443** 76–88
[20] Bardotti L, Jensen P, Horeau A, Treilleux M and Cabaud B 1995 *Phys. Rev. Lett.* **74** 4694–7
[21] Carroll S J, Pratontep S, Streun M, Palmer RE, Hobday S and Smith R 2000 *J. Chem. Phys.* **113** 7723–7
[22] Van Hardeveld R and Hartog F 1969 *Surf. Sci.* **15** 189–230
[23] Baker S H, Roy M, Gurman S J, Louch S, Bleloch A and Binns C 2004 *J. Phys.: Condens. Matter*. **16** 7813–21
[24] Baker S H, Roy M, Gurman S J, Louch S and Binns C 2005 *J. Phys.: Condens. Matter*. submitted
[25] Negrier M, Tuaillon-Combes J, Dupuis V, Melinon P, Perez A and Traverse A 2001 *Phil. Mag.* A **81** 2855
[26] Jamet M, Dupuis V, Melinon P, Guiraud G, Perez A, Wernsdorfer W, Traverse A and Baguenard B 2000 *Phys. Rev.* B **62** 493–9
[27] Binns C, Maher M J, Pankhurst Q A, Kechrakos D and Trohidou K N 2002 *Phys. Rev.* B **66** 184413
[28] Binns C and Maher M J 2002 *New J. Phys.* **4** 85
[29] O' Grady K and Bradbury A 1983 *J. Magn. Magn. Mater*. **39** 91–94
[30] Jamet M, Wernsdorfer W, Thirion C, Dupuis V, Melinon P, Perez A and Mailly D 2004 *Phys. Rev.* B **69** 024401
[31] Xie Y and Blackman J 2004 *J. Phys.: Condens. Matter*. **16** 3163–72
[32] Dimitrov D A and Wysin G M 1996 *Phys. Rev.* B **54** 9237–41
[33] Kechrakos D and Trohidou K N 1998 *Phys. Rev.* B **58** 12169–77
[34] Allia P, Coisson M, Tiberto P, Vinai F, Knobel M, Novak M A and Nunes W C 2001 *Phys. Rev.* B **64** 144420
[35] Kechrakos D and Trohidou K N 2000 *Phys. Rev.* B **62** 3941–51
[36] Edmonds K W, Binns C, Baker S H, Thornton S C, Norris C, Goedkoop J B, Finazzi M and Brookes N B 1999 *Phys. Rev.* B **60** 472–6
[37] Edmonds K W, Binns C, Baker S H, Thornton S C and Finetti P 2000 *J. Appl. Phys*. **88** 3414
[38] Chado I, Padovani S, Scheurer F and Bucher J-P 2000 *Appl. Surf. Sci*. **164** 42–7
[39] Chudnovsky E M 1983 *J. Magn. Magn. Mater.* **40** 21
[40] Chudnovsky E M, Saslow W M and Serota R A 1986 *Phys. Rev.* B **33** 251–61
[41] Saslow W M 1987 *Phys. Rev.* B **35** 3454–60
[42] Chudnovsky E M 1988 *J. Appl. Phys*. **64** 5770
[43] Chudnovsky E M 1995 *The Magnetism of Amorphous Metals and Alloys* vol 80 (*Springer Series in Solid-State Sciences*) ed J A Fernandez-Baca and Wai-Yim Ching (Singapore: World Scientific)
[44] Loffler J F, Meier J P, Doudin B, Ansermet J-P and Wagner W 1998 *Phys. Rev.* B **57** 2915–24
[45] Loffler J F, Braun H-B and Wagner W 2000 *Phys. Rev. Lett.* **85** 1990–3
[46] Thomas L, Tuaillon J, Perez J P, Dupuis V, Perez A and Barbara B 1995 *J. Magn. Magn. Mater.* **140** 437
[47] Perez J P, Dupuis V, Tuaillon J, Perez A, Paillard V, Melinon P, Treilleux M, Thomas L, Barbara B and Bouchet-Fabre B 1995 *J. Magn. Magn. Mater.* **145** 74
[48] Wiedwald U, Cerchez M, Farle M, Fauth K, Schütz G, Zürn K, Boyen H-G and Ziemann P 2004 *Phys. Rev.* B **70** 214412
[49] Berkowitz A E, Mitchell J R, Carey M J, Young A P, Zhang S, Spada F E, Parker F T, Hutten A and Thomas G 1992 *Phys. Rev. Lett.* **68** 3745–8
[50] Xiao J Q, Jiang J S and Chien C L 1992 *Phys. Rev. Lett.* **68** 3749–52

[51] Tsymbal E Y and Pettifor D G 2001 *Solid State Phys*. **56** 113–237
[52] Zhang S F and Levy P M 1993 *J. Appl. Phys*. **73** 5315–19
[53] Kechrakos D and Trohidou K N 2003 *Recent Res. Dev. Phys.* **4** 287–307
[54] Billas I M L, Becker J A, Châtelain A and De Heer W A 1993 *Phys. Rev. Lett.* **71** 4067–70
[55] Edmonds K W, Binns C, Baker S H, Maher M J, Thornton S C, Tjernberg O and Brookes N B 2000 *J. Magn. Magn. Mater.* **220** 25–30
[56] Palasantzas G, Kock S A and De Hosson J Th 2002 *Appl. Phys. Lett.* **81** 1089–91
[57] Baker S H, Binns C, Edmonds K W, Maher M J, Thornton S C, Louch S and Dhesi S S 2002 *J. Magn. Magn. Mater.* **247** 19–25
[58] Louch S 2005 *PhD Thesis* University of Leicester
[59] Di Fonzo F *et al* 2000 *Appl. Phys. Lett.* **77** 910
[60] Xie Y and Blackman J A 2005 submitted
[61] Bansmann J and Kleibert A 2005 *Appl. Phys.* A **80** 957–64
[62] Ebert H and Battocletti M 1996 *Solid State Commun.* **98** 785
[63] Chen C T, Idzerda Y U, Lin H-J, Smith N V, Meigs G, Chaban E, Ho G H, Pellegrin E and Sette F 1995 *Phys. Rev. Lett*. **75** 152–5
[64] Mpourmakis G, Froudakis G E, Andriotis A N and Menon M 2005 submitted
[65] Kortus J, Baruah T, Pederson M R, Ashman C and Khanna S N 2002 *Appl. Phys. Lett*. **80** 4193–5
[66] Tuaillon-Combes J, Négrier M, Barbara B, Wernsdorfer W, Treilleux M, Mélinon P, Boisron O and Perez A 2003 *Int. J. Nanosci.* **2** 75
[67] Malhotra S S, Liu Y, Shan Z S, Liou S H, Stafford D C and Sellmyer D J 1996 *J. Appl. Phys*. **79** 5958
[68] Dupuis V, Favre L, Stanescu S, Tuaillon-Combes J, Bernstein E and Perez A 2004 *J. Phys.: Condens. Matter.* **16** S2231–40
[69] Bansmann J *et al* 2005 *Surf. Sci. Rep*. **56** 189–275
[70] Dennler S, Morillo J and Pastor G M 2003 *Surf. Sci.* **532–535** 334–40
[71] Dennler S, Ricardo-Chavez J L, Morillo J and Pastor G M 2003 *Eur. Phys. J.* D **24** 237
[72] Guirado-Lopez R, Dorantes-Davila J and Pastor G M 2003 *Phys. Rev. Lett.* **90** 226402
[73] Felix-Medina R, Dorantes-Davila J and Pastor G M 2002 *New J. Phys*. **4** 100
[74] Felix-Medina R, Dorantes-Davila J and Pastor G M 2003 *Phys. Rev.* B **67** 094430
[75] Dorantes-Davila J, Dreyssé H and Pastor G M 2003 *Phys. Rev. Lett.* **91** 197206
[76] Guirado-Lopez R, Dorantes-Davila J and Pastor G M 2003 *Eur. Phys. J.* D **24** 73
[77] Munoz-Navia M J, Dorantes-Davila J and Pastor G M 2004 *J. Phys.: Condens. Matter.* **16** S2251–6
[78] Dennler S, Morillo J and Pastor G M 2004 *J. Phys.: Condens. Matter* **16** S2263–72
[79] Munoz-Navia M, Villasenor-Gonzalez P, Dorantes-Davila J and Pastor G M 2005 *Comput. Mater. Sci.* submitted
[80] Dennler S, Morillo J and Pastor G M 2005 submitted
[81] Munoz-Navia M, Dorantes-Davila J and Pastor G M 2005 submitted
[82] MeikleJohn W H and Bean C P 1956 *Phys. Rev.* **102** 1413
[83] Peng D L, Sumiyama K, Konno T J, Hihara T and Yamamuro S 1999 *Phys. Rev.* B **60** 2093–100
[84] Kuhn L T, Bojesen A, Timmermann L, Nielsen M M and Morup S 2002 *J. Phys.: Condens. Matter.* **14** 13551–67